



18 **Abstract**

19 The oceanic crust is initially cooled and deep-sea chemosynthetic ecosystems are largely fed by  
20 hydrothermal circulation and venting on the seafloor. Much of this venting takes place at mid-  
21 ocean ridges and in order to make realistic models of the crust's thermal budget and to  
22 understand chemosynthetic biogeography it is important to have a detailed inventory of vent  
23 sites. Until recently, a major gap in this inventory was the Mid-Atlantic Ridge south of 13°S, a  
24 key region for vent fauna biogeography as it is the corridor linking the Atlantic to the Indian and  
25 Pacific Oceans. In spring 2013 we systematically surveyed the axial region between 13°S and  
26 33°S for hydrothermal signals in the water column, using turbidity, oxidation-reduction-potential  
27 (ORP) and noble gases as indicators. Standard conductivity-temperature-depth (CTD) rosette  
28 water-sampler deployments were complimented by a novel autonomous underwater vehicle  
29 (AUV) deployment strategy, in which the AUV made single-pass, segment-scale (up to 100 km  
30 long) dives close to the seafloor to detect small vents. The ca. 2100 km-long survey covered 16  
31 ridge segments and we identified previously unknown hydrothermal plumes above ten segments  
32 that point to 14 new hydrothermal vent fields. The majority of plumes are located at high-relief  
33 segment centers, where magmatism is robust. A wide gap in the distribution of vents in the 19°S-  
34 23°S region coincides with the Rio de Janeiro Transform, the maximum southward progression  
35 of North Atlantic Deep Waters and the maximum northwards extent of <sup>3</sup>He-enriched waters with  
36 Pacific origins. Crossflowing currents in the transform and the large gap between adjacent vents  
37 may prevent a meridional connection between the vent fauna communities in the North Atlantic  
38 and along the Antarctic Ridges. This makes the region a prime target for future biogeographical  
39 studies.

## 40 **1 Introduction**

41 Hydrothermal venting along the globe-spanning network of mid-ocean ridges (MORs) is a key  
42 process for the transfer of chemical elements and heat from the lithosphere into the ocean. Knowing the  
43 location of individual vent fields, their frequency and spacing along the ridge axes, their discharge rates  
44 and fluid compositions is crucial to constrain geochemical cycles and the heat budget of the ocean crust  
45 (Edmond et al., 1979; Elderfield and Schultz, 1996; Hasterok, 2013; Saito et al., 2013). Hydrothermal vent  
46 sites represent oases in the deep sea, as the discharged dissolved and particulate chemicals fuel microbial  
47 chemosynthesis that nourishes endemic vent communities (Fisher et al., 2007; Van Dover et al., 2002).  
48 Determining the location of individual vent sites is a prerequisite to investigate the regional vent  
49 communities and to understand their geographic dispersal and genetic connectivity across different ocean  
50 basins (Kelley and Shank, 2010; Shank et al., 1998; Van Dover et al., 2002). Currently, there is a large  
51 geographical gap between known vents sites in the equatorial Atlantic and those along the Antarctic and  
52 Indian Ocean ridges, so the South Atlantic is a missing link in global biogeography and it is important to  
53 define biogeographic boundaries (Copley et al., 2016; Moalic et al., 2012). A further important aspect is  
54 the increasing commercial interest in hydrothermal vent sites, because they represent the location of  
55 formation of metal-rich seafloor massive sulfide deposits. Slow spreading MOR, such as the Mid-Atlantic  
56 Ridge, are expected to bear more than 80% of the known seafloor tonnage of seafloor massive sulfides  
57 (German et al., 2016; Hannington et al., 2011; Tivey, 2007).

58 Since the initial discovery of active hydrothermal vents and sulfide mounds at the axes of MORs  
59 in the late 1970s (Corliss et al., 1979; Rona et al., 1986) significant progress has been made in their  
60 oceanographic, geological and biological exploration. By mid-2018 the InterRidge Vents Database  
61 (Beaulieu et al., 2013) – the authoritative reference for the locations of active hydrothermal vent sites –  
62 lists 288 confirmed vent fields and 355 additional sites inferred from water column plume-surveys (Figure  
63 1; Beaulieu, 2015). However, large portions of the global MORs are still unexplored for hydrothermalism  
64 (Beaulieu et al., 2015). A prominent example is the Southern Mid-Atlantic Ridge (SMAR) south of 14°S  
65 which was, until 2013, a blank spot on the global map of venting (inset in Figure 1).

66 To better constrain geochemical fluxes related to hydrothermal venting, to define the  
67 biogeographic regions of endemic vent communities and to precisely evaluate associated massive sulfide  
68 deposits it is essential that we first determine the locations of active vent fields along the SMAR. Inferred  
69 vent locations will then serve as the basis for cruise planning and detailed studies of hydrothermalism  
70 along the SMAR in the future. In this paper we present the water column results from cruise MSM-25 of  
71 RV Maria S. Merian which took place in early 2013 with the primary goal of systematically surveying all  
72 ridge segments between 13°-33°S for hydrothermal venting (Devey and cruise-participants, 2013). We  
73 combine measurements from 11 dives of an autonomous underwater vehicle (AUV) with those from ship  
74 based hydrographic casts. Our approach is based on the detection of several independent tracers for  
75 hydrothermal venting: a) the oxidation-reduction potential (ORP), b) turbidity anomalies resulting from  
76 hydrothermal particles and c) primordial helium, expressed as  $\delta^3\text{He}$ , discharged into the ocean by vent  
77 fluids.

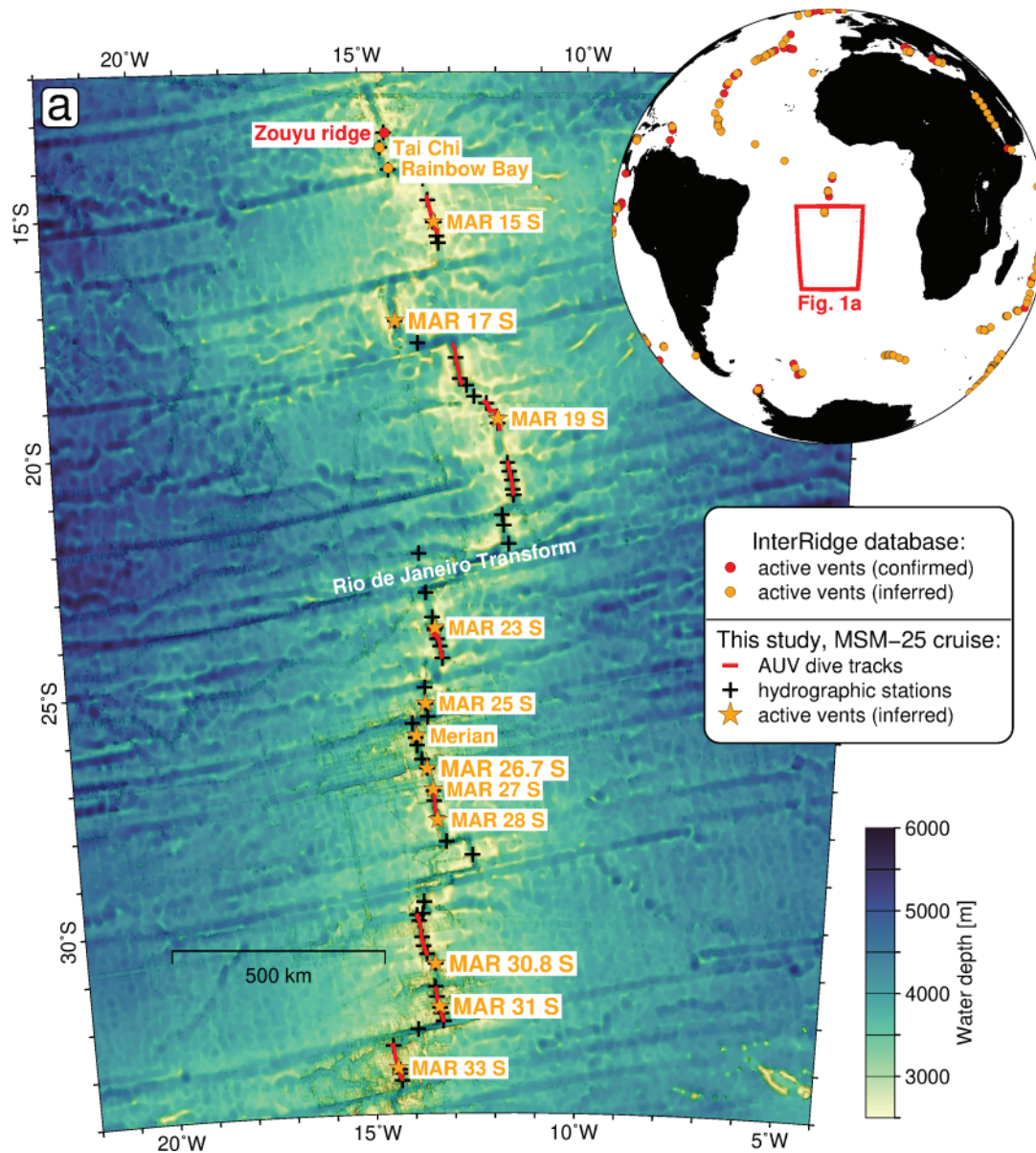


**Figure 1.** Map a, overview of the study area at the Southern Mid-Atlantic Ridge (SMAR) with locations of confirmed (red) and inferred (orange) active vent sites extracted from the InterRidge Vents Database, version 3.4 (<http://vents-data.interridge.org/>). Locations of hydrographic stations and inferred vent sites from the MSM-25 cruise are also given. Bathymetry from GMRT synthesis (Ryan et al., 2009). The globe in the upper right corner shows the location of the bathymetry map and further vent sites from the InterRidge database.

## 78 **2 Hydrothermalism at the Slow Spreading Mid-Atlantic Ridge**

79 With full spreading rates of 20-35 mm a<sup>-1</sup> (DeMets et al., 2010) the Mid-Atlantic Ridge is a slow  
80 spreading MOR. Slow spreading MORs make up ~60% of the total MOR system. The compilation of all  
81 known vent sites along the global MORs reveals a coincident increase in vent field incidence and  
82 spreading rate (Baker et al., 1996; Beaulieu et al., 2015). However, the incidence of vent sites along  
83 individual sections of the Mid-Atlantic Ridge is non-uniform and distance between sites varies over an  
84 order of magnitude (Beaulieu et al., 2015; German and Parson, 1998). German and Parson (1998) propose  
85 these variations are related to larger-scale variations in the interplay between magmatic and tectonic  
86 activity along the ridge. In a typical MOR setting, the primary heat source for hydrothermal venting are  
87 axial magma chambers, usually beneath the segment center (Baker and German, 2004; German and  
88 Parson, 1998). A higher incidence of vent sites along some ridge sections is attributed to deep penetrating  
89 faults, which enable heat mining from the lower crust/upper mantle (German and Parson, 1998).

90 Hydrothermal vents occur in various tectonic settings on the Mid-Atlantic Ridge in diverse  
91 lithologies ranging from basaltic hosted, e.g. Turtle Pits near 5°S (Haase et al., 2007), to ultramafic hosted  
92 e.g. Ashadze near 13°N (Fouquet et al., 2010). The diversity of host rock lithologies results in diversity in  
93 the vent fluid compositions (Edmonds, 2010) and vent faunal communities (Kelley and Shank, 2010).  
94 Slow- and ultraslow MORs have the highest diversity of hydrothermal systems of all MORs and since  
95 large portions of these ridges are still unexplored they represent highly promising grounds for future  
96 discoveries of vent sites with presently unknown characteristics (Baker, 2017; Beaulieu et al., 2015). In  
97 contrast to intermediate and fast spreading ridges, where hydrothermalism is limited to the narrow  
98 neovolcanic zone, can venting along slow spreading MORs occur far off-axis as in the case of Lost City  
99 (~15 km off-axis; Kelley et al., 2001) or the Nibelungen vent field at 8°S (~6 km off-axis; Melchert et al.,  
100 2008).

101 The relative sparsity of active vent sites along slow spreading ridges and the rough morphology  
102 make segment-scale tow surveys – as conducted along fast spreading, hydrothermally more active ridges  
103 (e.g. Baker et al., 2001; Baker et al., 2017) – very inefficient. Devey et al. (2010) proposed a conceptual  
104 model describing the interplay of volcanism, tectonics and hydrothermalism at slow spreading MORs.  
105 This model predicts that active venting is most likely to be detected at the magmatically robust axial highs  
106 where magma supply is enhanced and on geological time-scales only transiently disrupted by short  
107 sequences of tectonic activity. During the MSM-25 cruise we designed our survey strategy in reference to  
108 this conceptual model. Focused on morphologically pronounced axial highs, often coinciding with the  
109 segment's center and identified from ship-based multibeam bathymetry, the survey program included  
110 dedicated AUV dives and/or tow-yo casts to investigate these structures (Devey and cruise-participants,  
111 2013).

## 112 **3 Primordial (Mantle) Helium Emanating from MOR Hydrothermalism**

113 Lupton et al. (1977) were the first to report a massive plume of primordial helium (where the  
114 <sup>3</sup>He/<sup>4</sup>He ratio is significantly increased compared to the atmosphere) above the fast spreading East Pacific  
115 Rise originating from high-temperature hydrothermal venting. Owing to its inert nature the <sup>3</sup>He  
116 concentration in seawater is exclusively altered by dilution making it an ideal tracer for both hydrothermal  
117 activity and oceanographic processes (Jean-Baptiste et al., 2008; Lupton, 1998). <sup>3</sup>He anomalies persist  
118 over larger distances than particle plumes since the latter may be subject to scavenging, dissolution or  
119 particle fallout (Feely et al., 1994; Jean-Baptiste et al., 2008; Lupton and Jenkins, 2017). Plumes of <sup>3</sup>He  
120 above the northern Mid-Atlantic Ridge are weak ( $\delta^3\text{He}$  values do not exceed 15% outside regions in the  
121 immediate proximity of vent sites (Jean-Baptiste et al., 2008)). In comparison, at the fast spreading East  
122 Pacific Rise an extensive <sup>3</sup>He plume of  $\delta^3\text{He}$  values larger than 50% was observed up to 400 m above the  
123 ridge axis (Lupton, 1998). The lower <sup>3</sup>He above the Mid-Atlantic Ridge is due to a lower vent field  
124 incidence and the approximately 10 faster renewal rates of Atlantic deep waters than of Pacific deep  
125 waters which leads to an efficient removal of <sup>3</sup>He over the Mid-Atlantic Ridge (Jean-Baptiste et al., 2008).

126 Surveys of  $^3\text{He}$  have been successfully used to trace hydrothermal activity at regional and local  
127 scales on slow spreading MORs (Jean-Baptiste et al., 2004; Jean-Baptiste et al., 2008; Jean-baptiste et al.,  
128 1991). The discharge of  $^3\text{He}$  at the Mid-Atlantic Ridge is strongest at high-temperature magmatic-hosted  
129 hydrothermal systems and generally weaker at, low-temperature cumulate- or mantle-hosted systems, e.g.  
130 Lost City and Ashadze (Charlou et al., 1998; Edmonds, 2010; Jean-Baptiste et al., 2008; Keir et al., 2006).  
131 First indications for active venting along the southern MAR came from large scale  $^3\text{He}$  distributions  
132 obtained on sections World Ocean Circulation Experiment (Rüth et al., 2000), where  $^3\text{He}$  far field plume  
133 signals emanating from the ridge crest were observed between 11°S and 30°S.

## 134 **4 Materials and Methods**

### 135 **4.1 Ship and AUV Based Plume Surveying**

136 We deployed five Pacific Marine Environmental Laboratory (PMEL) Miniature Autonomous  
137 Plume Recorders (MAPRs) equipped with turbidity, oxidation-reduction potential (ORP), temperature and  
138 pressure sensors. For standard vertical casts one MAPR unit was mounted to the SeaBird Electronics  
139 911plus conductivity-temperature-depth (CTD) probe. For tow-yo stations additional MAPR units were  
140 mounted on the cable roughly 50, 100, 150 and 200 m above the CTD. The MAPR turbidity sensor is a  
141 custom built, high-sensitivity optical backscatter sensor (Seapoint Sensors, Inc) that is specifically tuned  
142 to identify plumes of hydrothermal particles, typically discharged by hydrothermal vents of exit  
143 temperatures  $> 100^\circ\text{C}$  (Baker et al., 2016). Turbidity is measured in dimensionless nephelometric turbidity  
144 units (NTU) and reported here as the anomaly ( $\Delta\text{NTU}$ ) above ambient background seawater. ORP  
145 anomalies are caused by nanomolar concentrations of reduced hydrothermal chemicals (e.g.  $\text{Fe}^{2+}$ ,  $\text{HS}^-$ ,  $\text{H}_2$ )  
146 which are rapidly oxidized or metabolized after being discharged into the ocean (Walker et al., 2007).  
147 ORP anomalies typically occur closer to the vent site than turbidity anomalies and thus are a good  
148 indicator of active venting within  $\sim 1\text{-}2$  km (Baker et al., 2016; Baker et al., 2017). The ORP sensor  
149 response is characterized by a steep decrease in potential once a plume anomaly is intersected, followed  
150 by a gradual recovery (Baker et al., 2016). Absolute potential values,  $E$ , given by the ORP sensor may  
151 vary between individual sensors due to sensor drift or hysteresis. Therefore, the time derivative  $dE/dt$  is  
152 used to define an ORP anomaly ( $\Delta E$ ) whenever  $dE/dt$  is more negative than  $-0.02$  mV for consecutive  
153 measurements and the total drop in voltage is  $> 1.0$  mV. By applying these thresholds we avoid  
154 ambiguous signals caused by the variable nature of the background values. The AUV was also equipped  
155 with turbidity and ORP sensors.

156 During the MSM-25 cruise we conducted hydrographic casts at all high-relief segment centers  
157 identified from topography and additional casts at segment-ends of all 16 first-order ridge segments  
158 between 13-33°S. The AUV accomplished nine long-range missions during which the vehicle was  
159 programmed to survey at 150 m altitude and two dedicated dives above the Zouyu Ridge (13°S) and the  
160 Merian vent field (26°S) were carried out at 50 m altitude.

161

### 162 **4.2 Sampling and Analysis of Helium Isotopes**

163 For the analysis of helium isotopes in the waters above the SMAR two different sampling  
164 methods were used (Devey and cruise-participants, 2013). 522 samples were filled into pinched-off copper  
165 tubes that were sealed free of head space and 451 samples were drawn into evacuated glass ampoules by  
166 leaving a head space for gas phases, following the methodology of Roether et al. (2013). After the cruise  
167 all samples were further processed and analysed in the Bremen Helium Isotope Laboratory (Helis;  
168 Sültenfuß et al., 2009). After gas extraction (only necessary for copper tube samples) the gases are  
169 analysed with a fully automated mass spectrometry facility, of which the technical details are provided in  
170 Sültenfuß et al. (2009). 973 samples were successfully analysed and the achieved noble gas dataset  
171 (including concentrations of  $^3\text{H}$ ,  $^4\text{He}$ ,  $\text{Ne}$ ) was carefully checked for spurious values, by also considering  
172 neon. We discard all samples that show a  $\Delta(\text{Ne})$  value lower than 1% and higher than 8% as values

173 outside this range are implausible (Well and Roether, 2003). The neon data were further used to correct  
174 for excess air in the samples caused by wave induced bubble injection, melting ice or contamination,  
175 following the approach of (Roether et al., 2001); Roether et al. (1998). Details of excess air correction are  
176 provided in Supporting Information Texts S1-S3. In the following we present helium data as excess air  
177 corrected values in the commonly used delta notation,  $\delta^3He = \left( \frac{R}{R_a} - 1 \right) 100$ , where  $R$  is the  $^3He/^4He$  ratio  
178 in the sample and  $R_a$  is the  $^3He/^4He$  ratio in the atmosphere.

### 179 **4.3 Bathymetry Data and Underwater Positioning**

180 Bathymetric data were acquired with a hull-mounted Kongsberg EM122 echosounder. The raw  
181 data were manually cleansed of outliers and grids of 50 m horizontal resolution were produced for each  
182 surveyed ridge segment. Wherever available, the bathymetry grids were supplemented with auxiliary ship-  
183 based data from the Global Multi-Resolution Topography Synthesis archive (Ryan et al., 2009). A hull-  
184 mounted ultra-short baseline system (USBL, IXSEA “Posidonia”) was used for precise positioning of the  
185 CTD rosette and MAPRs during tow-yo stations. The AUV operated during the cruise (GEOMAR’s  
186 REMUS 6000 vehicle “ABYSS”) is equipped with an inertial navigation system and a USBL beacon. The  
187 inertial navigation system gives relative positions during the dive while the USBL allowed us to determine  
188 the vehicles absolute position whenever the ship was in proximity during the dives. For each dive at least  
189 two independent USBL position fixes (typically when the AUV had arrived at the bottom and at a later  
190 stage before the vehicle departed from the bottom) were achieved (Devey and cruise-participants, 2013).  
191 Using these fixes, the horizontal drift of the inertial navigation system was determined and yielded  
192 deviations within 100–900 meters after a 12-18 h dive. The AUV navigation data was shifted accordingly  
193 in post processing.

### 194 **4.4 Current Velocity Measurements and Predicted Barotropic Tidal Velocities**

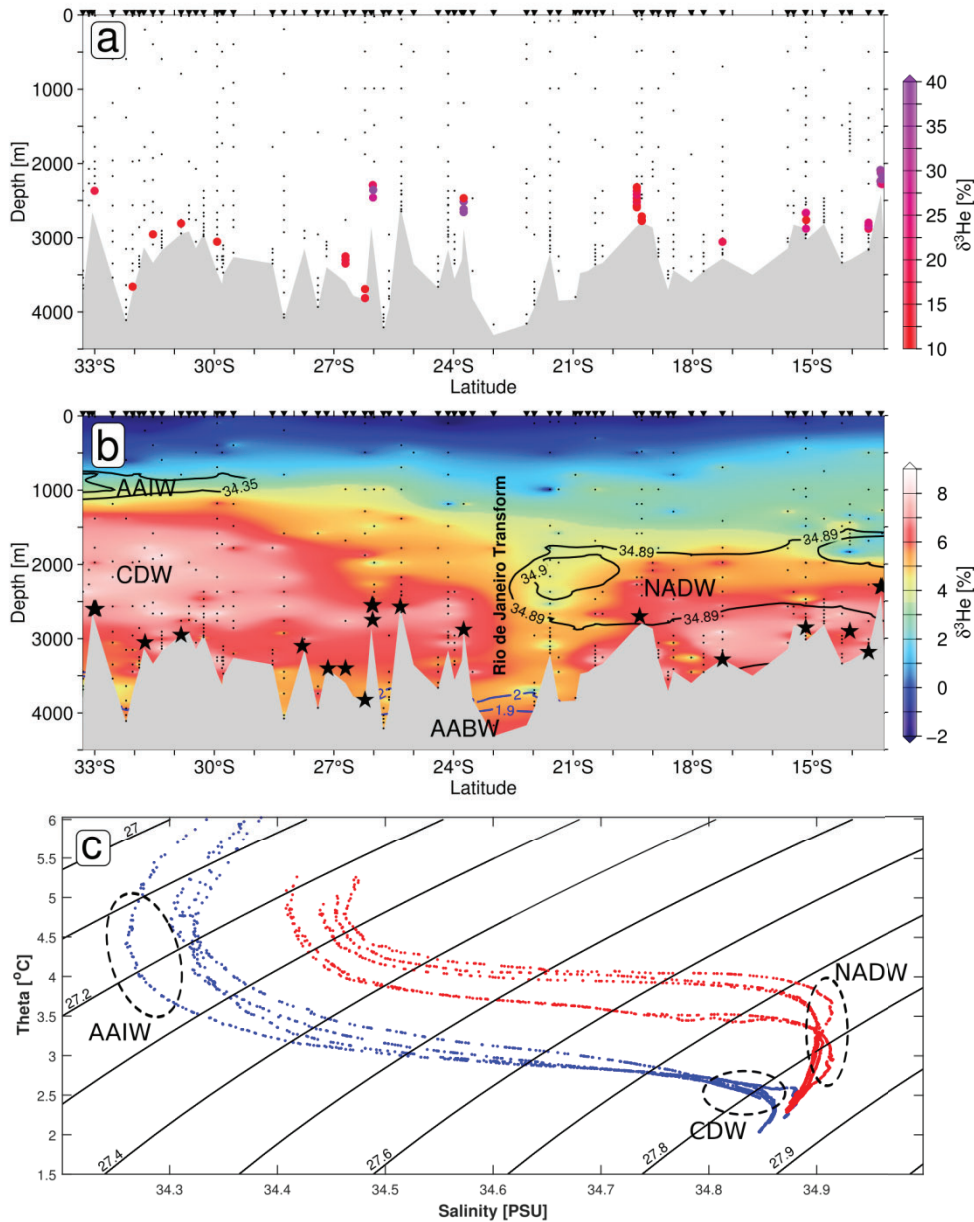
195 Current velocities were measured with two RDI Workhorse lowered Acoustic Doppler Current  
196 Profilers, mounted to the CTD-rosette water sampler (Devey and cruise-participants, 2013). One sensor  
197 faced downwards and the second one upwards and both instruments were operated in synchronous mode,  
198 recording average velocities in 10 m vertical bins. The current velocity data were processed following the  
199 scheme of Visbeck (2002). In this study we only use measurements from near the seafloor (less than 300  
200 m above bottom), gathered via the instruments bottom-tracking mode. The amplitudes and directions of  
201 predicted barotropic tidal velocities for the location and the operation period of selected CTD stations  
202 were retrieved from the global model of ocean tides prediction, TPXO7.1, developed by Egbert and  
203 Erofeeva (2002).

## 204 **5 Results and Discussion**

### 205 **5.1 $^3He$ above the SMAR axis**

206 The analysis and quality control of noble gas data yielded 525 discrete  $\delta^3He$  values above the  
207 SMAR axis (Figure 2), a survey which is unprecedented in its extent along the spreading axis and density  
208 of sampling in the bottom waters.  $\delta^3He$  ranges between -3.4 % and 146.9 % with negative values only  
209 present at depths shallower than 2000 m (Figure 2b) and values > 10 % only occurring at discrete sites  
210 deeper than 2000 m (Figure 2a). The general pattern of  $\delta^3He$  values above the SMAR suggests that the  
211 oceanic background in the different water masses does not exceed 10 % and all values above this  
212 threshold may thus be considered affected by hydrothermal input (Figure 2). Our meridional transect of  
213 background  $\delta^3He$  (omitting all values of  $\delta^3He > 10$  %, Figure 2b) is in agreement with the cross-cutting  
214 zonal transects of  $\delta^3He$  at 19°S and 30°S presented in Roether et al., (1998) and R uth et al., (2000). The  
215 published zonal section at 19°S shows a  $\delta^3He$  maximum of 5.5% directly above the SMAR axial seafloor  
216 and ~2000 m depth (R uth et al., 2000) which is consistent with our dataset (Figure 2b). The zonal section  
217 at 30°S shows a slightly stronger maximum of 7% that reaches from the seafloor up to 1000 m depth as

218 does our data (Figure 2b; R uth et al., 2000). Overall, the <sup>3</sup>He values are of similar magnitude with those  
 219 above the Northern Mid-Atlantic Ridge and lower than those above the fast Spreading East Pacific Rise  
 220 (Lupton, 1998).



221

**Figure 2.** Two aspects of the <sup>3</sup>He distribution above the SMAR. Panel a shows samples as colored circles where <sup>3</sup>He is larger than 10%, which are considered as hydrothermally sourced anomalies. Small black dots show all sampling locations that yielded reliable <sup>3</sup>He values after quality control. Panel b shows a gridded meridional section <sup>3</sup>He. Values of <sup>3</sup>He < 9% have been omitted from gridding and thus the image represents the oceanic background in <sup>3</sup>He, which is not immediately affected by hydrothermalism. Black contours delineate salinities > 34.89 psu, indicative of North Atlantic Deep Water (NADW). Blue contours delineate Antarctic Bottom Waters (AABW) of potential temperatures < 2.0 °C. CDW denotes Circumpolar Deep Waters carrying excess <sup>3</sup>He from the Pacific. Black stars indicate locations of identified hydrothermal vent sites. Panel c, T-S diagram for stations south of the Rio de Janeiro Transform (blue) and

stations north of the Transform (red). Contours represent isopycnals. Data shallower than 700 dbar have been omitted. Note, that different water masses of AAIW, NADW and CDW occupy distinct temperature and salinity ranges.

## 222 **5.2 Is the Rio de Janeiro Transform (22°S) a Barrier to the Meridional Dispersal of Vent** 223 **Fauna?**

224 The Rio de Janeiro Fracture Transform valley at 22°S represents the deepest cross-passage in the  
225 survey area and is associated with a ~220 km offset in the ridge axis. The fracture zone coincides with a  
226 gap in the distribution of hydrothermal vent fields between 19°S - 23°S and is marked by a decrease of  
227 <sup>3</sup>He concentrations throughout the water column (Figure 2b). Our hydrographic data from the SMAR axis  
228 indicate that the southward progression of North Atlantic Deep Waters (NADW) is interrupted above this  
229 region (Figure 2b,c). Waters at 1000-2500 m depth in the region south of 27°S represent Circumpolar  
230 Deep Waters (CDW) that are enriched in <sup>3</sup>He ( $\delta^3\text{He} > 6\%$ ) due to the elevated <sup>3</sup>He background from the  
231 Pacific entering the South Atlantic via the Drake Passage (Rüth et al., 2000; Well et al., 2003). Mercier et  
232 al. (2000) report a throughflow in the Rio de Janeiro Transform supplied by cold and fresh bottom waters  
233 from the deep basins west of the SMAR. This is supported by our hydrographic measurements revealing  
234 Antarctic Bottom Waters (AABW) identifiable from potential temperatures < 2.0 °C (Broecker et al.,  
235 1976) in the deepest part of the transform valley (Figure 2b).

236 The along-axis dispersal success of passive larvae and microbes endemic to hydrothermal vents is  
237 dependent on bottom currents and the frequency of vent sites (McGillicuddy et al., 2010; Mullineaux et  
238 al., 2002). The crossflowing waters and the absence of active vents in the 19°-23°S region prevent the  
239 meridional dispersal of vent endemic larvae. The maximum southward progression of NADW suggests  
240 that larvae from the northern and Equatorial MAR may not be transported further south than the Rio de  
241 Janeiro Fracture Zone. We hypothesize that the topographic controlled hydrography and the sparse  
242 distribution of active vents in the 19°-22°S region constitute a physical barrier to the meridional dispersal  
243 and genetic connectivity between the different vent fauna communities found along northern MAR and  
244 the Circum-Antarctic Ridges (Copley et al., 2016; Moalic et al., 2012). However, this hypothesis may only  
245 be validated by biological investigations of the vent fauna immediately north and south of the Rio de  
246 Janeiro Transform.

## 247 **5.3 Detailed description of individual plume sites**

248 The following section describes in detail the individual plumes observed in geographical order  
249 from north to south. We also discuss the locations of underlying vent sites and their tectonic setting. A  
250 comprehensive summary of the coordinates of all the vent sites is provided in Table 1.

### 251 **5.3.1 Zouyu Ridge, 13°16'S**

252 The unusually extensive axial volcanic high near 13°16'S (Zouyu Ridge) was targeted by one  
253 AUV mission at 50 m altitude and tow-yo station 124 (Figure 3a, b). The axial high measures  
254 approximately 20 km along-axis by 8 km across-axis and rises as high as the local rift flanks (Figure 3a,  
255 b). Tow-yo 124 started at the western rim of the axial high and after pursuing a southeasterly heading for 3  
256 km the course was altered to north and the CTD was towed across a N-S oriented chain of up to 100 m  
257 high mounds sitting on top of a linear scarp (possibly fault or volcanic fissure; Figure 3b). The S-N  
258 oriented limb of the tow-yo crossed the previously known Zouyu-2 vent field (Figure 3b, e; Tao et al.,  
259 2011; Tao et al., 2017). The CTD sensor encountered a buoyant hydrothermal plume ~1 km south of the  
260 Zouyu-2 location (at 13°17.31'S/14°24.59'W; Figure 3e, f) marked by a temperature anomaly of +0.31 °C  
261 and strong density inversions between 2165-2210 m depth (Figure 3f).

262 An extensive neutrally buoyant plume was observed at ~200 m above the seafloor (Figure 3d, e).  
263 The plume increases slightly in vertical extent at the northern end of tow-yo 124, possibly due to venting  
264 near the Zouyu-1 vent field (Figure 3b). Increased turbidity in the bottom waters near the southern apex of

265 the tow-yo is consistent in both, MAPR and AUV data (Figure 3b, d-e) and may indicate the presence of  
266 several active chimneys near the identified buoyant plume. Widespread ORP anomalies were observed in  
267 the upper part of the particle plume, ~50 m above the layer of highest turbidity (Figure 3d, e). Occasional  
268 ORP anomalies were also observed below the particle plume, above the Zouyu-2 site, in the buoyant  
269 plume and near the western rim of the axial high (Figure 3d, e). The stratification above the axial high  
270 shows a staircase pattern as indicated by the variable spacing of isopycnals (Figure 3d, e and Supporting  
271 Information Figure S2) and the shape of the density profile in Figure 3f at depths shallower than 2160 m.  
272 Water samples along the tow-yo track yielded  $\delta^3\text{He}$  values of 22.9-47.9 ‰ in the neutrally buoyant plume  
273 and an exceptionally high value of 146.9 ‰ in bottle number 6 directly above the buoyant plume (Figure  
274 3e, f). Average current velocities in the near bottom layers range from 5–17 cm s<sup>-1</sup> and show a gradual  
275 change in direction along the tow-yo track, i.e. through time of measurement (Figure 3c). Predicted  
276 barotropic tidal velocities for this region, at the time of tow-yo operations, range from 3-5 cm s<sup>-1</sup> and show  
277 a gradual change in direction coinciding with measured near-bottom current velocities (Figure 3c).

278 The coordinates of Zouyu-2 from Tao et al. (2011), do not refer to an active vent but give the  
279 dredging location of a chimney fragment. Based on tow-camera observations Tao et al. (2011) estimated  
280 the vent field to have an extent of ~1 km in the N-S direction which suggests the hydrothermal discoveries  
281 of Tao et al. (2011) in 2009/2011 and the buoyant plume we discovered in 2013 relate to the same vent  
282 field, Zouyu-2. ORP signals are indicative of recently discharged hydrothermal fluids (Walker et al.,  
283 2007), suggesting the neutrally buoyant plume is particularly ‘fresh’ in its uppermost layers (Figure 3d, e).  
284 The current velocity measurements suggest that tides rapidly spread the plume waters across the axial  
285 high. Similar types of advection of hydrothermal plumes by tides and background currents have been  
286 described at other sites on the MAR, such as above the Logachev vent field (Schmale et al., 2012) or the  
287 Nibelungen vent field (Walter et al., 2010).

288 A constant vertical offset between an ORP plume and a particle plume is unusual and has never  
289 before been observed above any active vent site in such clarity. As the number of active vent sites on the  
290 Zouyu Ridge and their chemistries are unknown we can only speculate about the cause of this vertical  
291 offset. We present two scenarios to explain this offset. In the first scenario, the Zouyu-2 vent field is the  
292 primary source of the neutrally buoyant plume and the upper layer of anomalous ORP and low turbidity  
293 represents the freshest portion of the plume while the lower layer of highest turbidity and without ORP  
294 signal is composed of mature plume waters. Such a layering could be sustained by gravitational separation  
295 of hydrothermal particles from the reduced chemicals (e.g. Fe<sup>2+</sup>, HS<sup>-</sup>, H<sub>2</sub> producing the ORP signal)  
296 supported by the staircase stratification. The settling of particles is retarded by a jump in density (crossing  
297 the 36.992 kg m<sup>-3</sup> isopycnal, Figure 3d-f and Supporting Information Figure S1). The vertical offset may  
298 also result from overshooting of the buoyant plume waters in the wake of which particles fall back to a  
299 level of higher density than the reduced chemicals. In the second scenario, the neutrally buoyant plume is  
300 fed by two separate venting sites of different characteristics. Site A (possibly the one producing the  
301 observed buoyant plume) discharges particle-rich fluids that are poor in reduced chemicals and thus  
302 produce no ORP anomalies beyond the buoyant plume. Site B is rich in reduced chemicals, poorer in  
303 particles and either located at shallower depths (possibly on one of the ~100 m high mounds) or has higher  
304 exit temperatures than site A in order to produce a plume of ~50 m higher rise height.

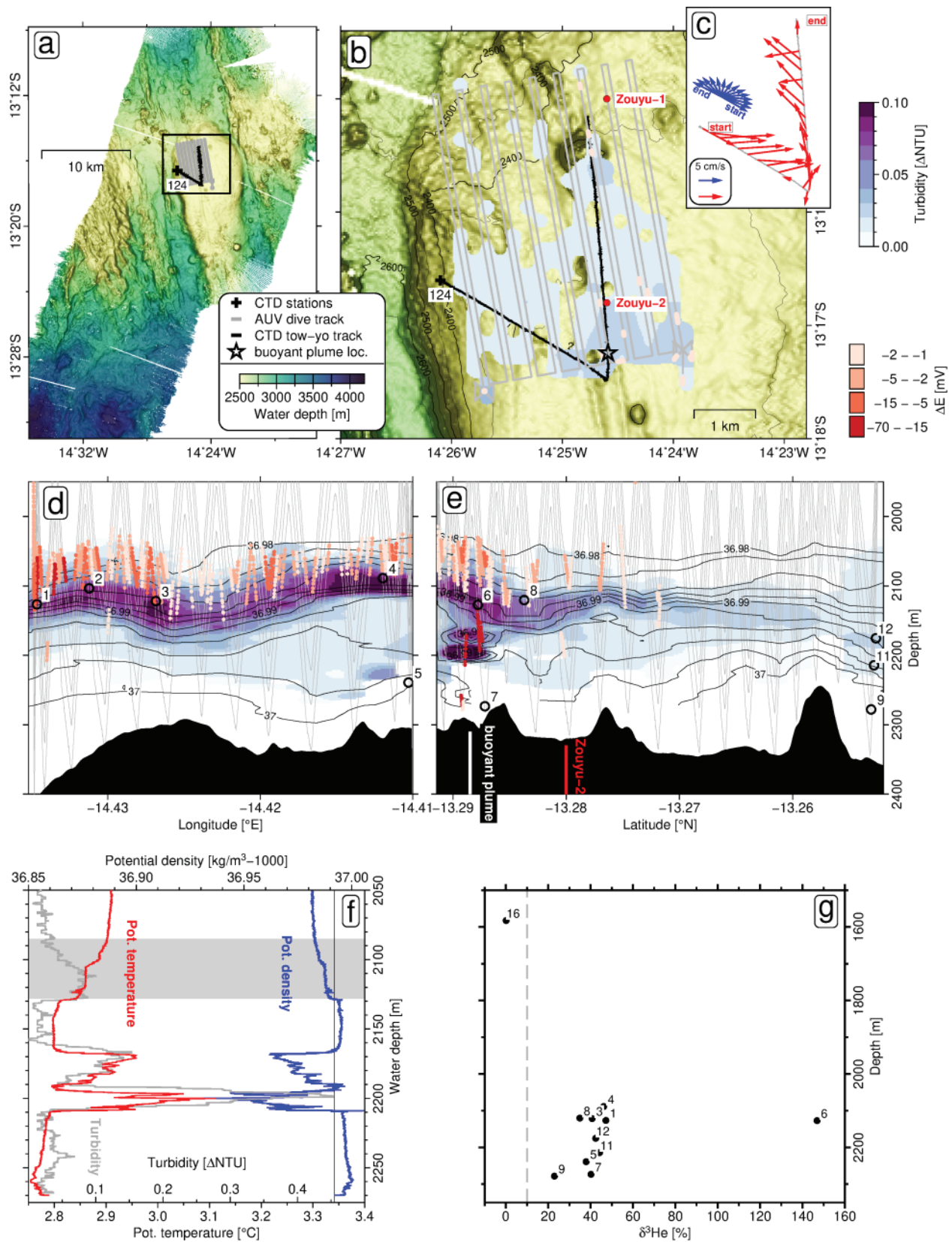
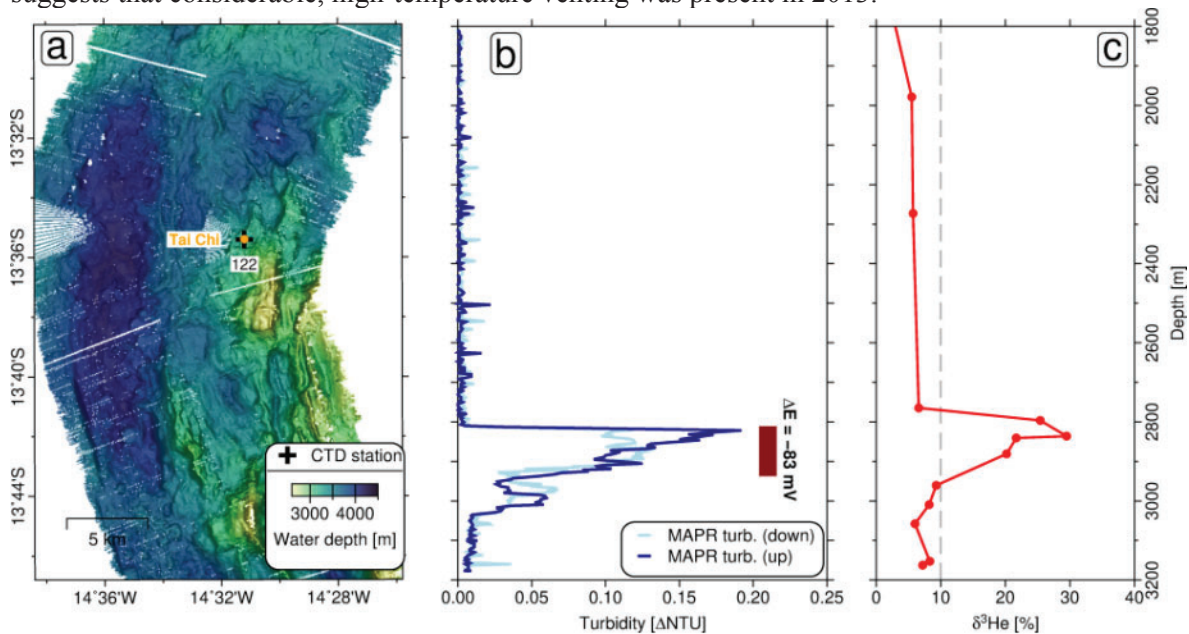


**Figure 3.** Plume results from the Zouyu Ridge. Panel a, bathymetry overview of the segment. The black rectangle indicates perimeter of map b. Detailed map b shows the flat-topped axial high

hosting the Zouyou-1 and 2 vent fields, coordinates from Tao et al. (2017). The gray shading represents gridded AUV turbidity, at the same color scale as MAPR data in panels d and e. Note, the AUV was flown at 50 m above seafloor and thus remained below the main turbidity plume. Panel c, vectors of measured current velocities, red, along the tow-yo track and predicted barotropic tidal current velocities, blue. Panels d and e show results from tow-yo station 124 separately for the NE-SW and S-N striking parts of the station, respectively (tow track is plotted on map b). Faint gray lines indicate MAPR tracks, blue shading scales with turbidity, red dots show  $\Delta E$  anomalies. Numbered circles show water sampling locations and black contours are isopycnals calculated from CTD data. Panel f, profiles of temperature, density and turbidity of the CTD sensor for the tow-yo up-cast crossing the buoyant plume. To correct for a delayed response of the CTD-mounted turbidity sensor, the signal was shifted 3 m upwards before plotting. The gray shaded area indicates the depth of the neutrally buoyant particle plume and the vertical black line shows the  $36.992 \text{ kg m}^{-3}$  isopycnal, coinciding with the lower boundary of the particle plume. Panel g,  $\delta^3\text{He}$  results from station 124 with labels corresponding to bottle numbers in panels d and e.

### 306 5.3.2 Tai Chi Vent Field, 13°36'S

307 Vertical CTD station 122 above the previously known Tai Chi vent field (also spelled Taiji;  
 308 Figure 4a) located at approximately 3100 m water depth on the northern face of an inside corner high  
 309 marking the southern boundary of a non-transform ridge-offset (Li et al., 2018). Turbidity and ORP  
 310 anomalies were found between 2810 – 2950 m depth (Figure 4b). The upper boundary of the plume is  
 311 sharply defined and correlates with a maximum  $\delta^3\text{He}$  value of 29.5 ‰ (Figure 4c). Li et al. (2018) reported  
 312 a weak temperature anomaly at 3000-3050 m depth, above the vent field in 2011. Their camera surveys  
 313 did not find sites of active discharge, leading to the conclusion that only diffusive venting was present in  
 314 2011. However, our discovery of a plume rich in  $^3\text{He}$ , particles and of reduced ORP  $\sim 200$  m higher  
 315 suggests that considerable, high-temperature venting was present in 2013.



316 **Figure 4.** Results from the Tai Chi vent field. Bathymetry map a shows the location of the Tai Chi vent field above which CTD station 122 was located. Panel b, MAPR turbidity and  $\Delta E$  anomalies (red bar) at station 122. Panel c, vertical profile of  $\delta^3\text{He}$  at station 122.

### 5.3.3 Deyin-1 Vent Field, MAR 15°10'S

318 The 14°6'S - 15°30'S segment was investigated by a long-range AUV mission which revealed  
 319 turbidity and ORP anomalies around 15°9.97'S/13°21.34'W and subsequently this site was further  
 320 investigated by tow-yo station 116 (Figure 5). In 2011 a plume had been observed at the same site by a  
 321 Chinese hydrothermal survey (S Wang et al., 2017) although this was unpublished at the time of the  
 322 MSM-25 cruise. The site is located on a ~200 m high neovolcanic ridge in the center of the axial valley  
 323 which was crossed from east to west by tow-yo 116 (Figure 5a, b). We mapped a particle plume at 2440-  
 324 2800 m depth extending to east and west of the neovolcanic ridge (Figure 5e). An ORP anomaly was  
 325 exclusively detected to the west, suggesting the active vent field is located on this side at ~2850 m depth.  
 326 Water samples 2 and 4 (Figure 5e, f) collected within the particle plume yield  $\delta^3\text{He}$  values of 25.9 % and  
 327 waters from slightly outside the particle plume (bottle numbers 5,7) fall back to the oceanic background  
 328 (Figure 5e). None of the monitored hydrothermal tracers showed an anomaly at the nearby station 113,  
 329 implying that this plume is locally confined. Dredged rock samples from this site yielded basalts and  
 330 massive sulfides (H Wang et al., 2017).

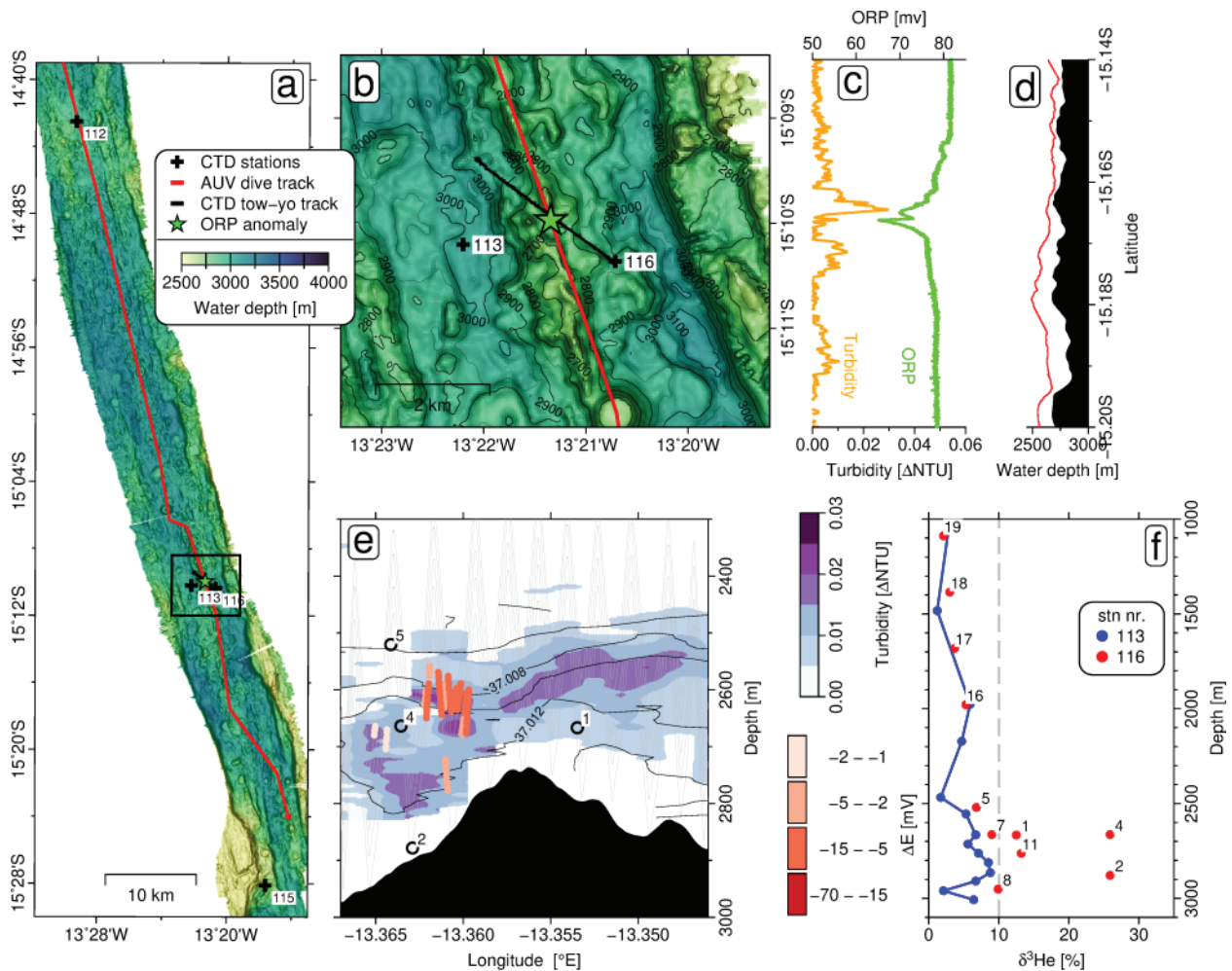


**Figure 5.** Results from the Deyin-1 site. Map a, bathymetry of the segment with black frame indicating the perimeter of map b. Panel c, turbidity and ORP measured along the AUV track on map b, plotted versus latitude. Panel d shows vehicle and seafloor depths versus latitude. Panel e, results from tow-yo station 116 with faint gray lines indicating MAPR tracks, blue shading representing turbidity and red dots showing  $\Delta E$  anomalies. Numbered circles show water sampling locations and black contours are isopycnals. Panel f,  $\delta^3\text{He}$  results from station 113 and

116 with labels corresponding to bottle numbers in panel e. Note, nearby CTD cast 113 did not see any hydrothermal anomaly.

331 **5.3.4 MAR 17° S**

332 The segment between 16°24'S and 17°36'S was sampled by vertical CTD station 107, located  
 333 above an axial high at the segment center. There, the axial valley is unusually narrow, 1.5 km wide,  
 334 compared to ~10 km width further north and south (Figure 6a). An  $\Delta E$  anomaly of -21 mV was detected  
 335 between 3010 and 3015 m depth (~260 m above the seafloor) but no significant increase in turbidity was  
 336 observed (Figure 6b). One water sample from 3055 m depth yielded a  $\delta^3\text{He}$  value of 19.9 ‰ confirming  
 337 the presence of hydrothermal input in the area (Figure 6c). The ORP anomaly implies that the source is  
 338 not far (< 1 km) from the sampling site and the absence of a turbidity anomaly suggests that venting is  
 339 likely of low-temperature and particle-poor character.

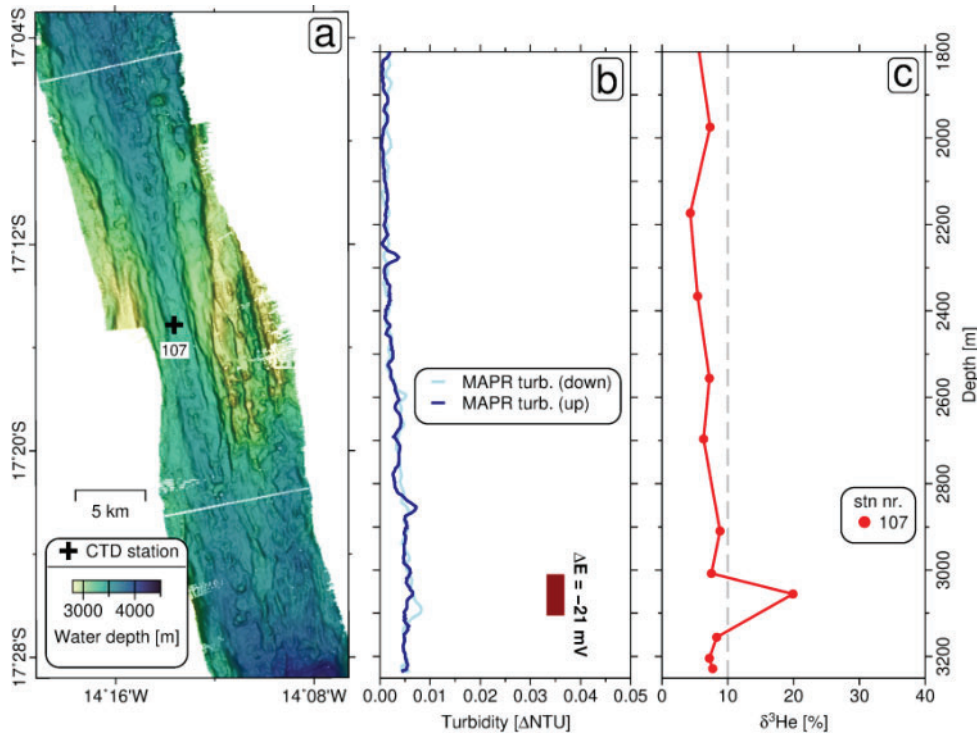


**Figure 6.** Results from the 17°S plume site. Map a, bathymetry map with location of CTD 10. Panel b, turbidity and depth of  $\Delta E$  anomaly at station 107. Panel c, profile of  $\delta^3\text{He}$  for station 107.

340 **5.3.5 MAR 19° S**

341 The SMAR axis between 19°S and 19°36'S, comprising several second-order ridge segments, was  
 342 surveyed by one long-range AUV mission and three vertical CTD casts. In this region the ridge axis is  
 343 characterized by a ~5 km wide axial valley that is, in most places, not significantly deeper than the ridge  
 344 flanks and bears numerous volcanic mounds (Figure 7a). During the AUV mission a 0.08  $\Delta\text{NTU}$  turbidity  
 345 anomaly was observed near 19°20.82'S/11°56.4'W in 2470 m water depth (Figure 7a-c) and an ORP  
 346 anomaly of -20 mV was observed at 19°19.8'S/11°56.52'W in 2585 m water depth, approximately 1.2 km  
 347 north of the turbidity anomaly. No turbidity or ORP anomalies were detected at tow-yo station 102 (~10  
 348 km south of the AUV ORP anomaly) and CTD cast 103 (~6 km north of the AUV ORP anomaly).  
 349 However, at both sites the  $\delta^3\text{He}$  values exceeds the oceanographic background with the highest value of  
 350 22.8 ‰ occurring at 2420 m water depth at station 102 (Figure 7d).

351 Most of the anomalies can be explained by the presence of a single hydrothermal field and  
 352 predominantly southwards directed currents in the area. The vent field's potential location is near the  
 353 maximum ORP anomaly, with the neutrally buoyant plume spreading at water depth between 2400 and  
 354 2600 m, where the maxima in turbidity and  $\delta^3\text{He}$  occur. Background  $\delta^3\text{He}$  values in the 2400-2600 m  
 355 depth interval at station 103 (Figure 7d) support the hypothesis that the plume is mainly dispersed to the  
 356 south and the minor  $\delta^3\text{He}$  anomaly below 2700 m depth at this site may indicate another hydrothermal  
 357 plume.

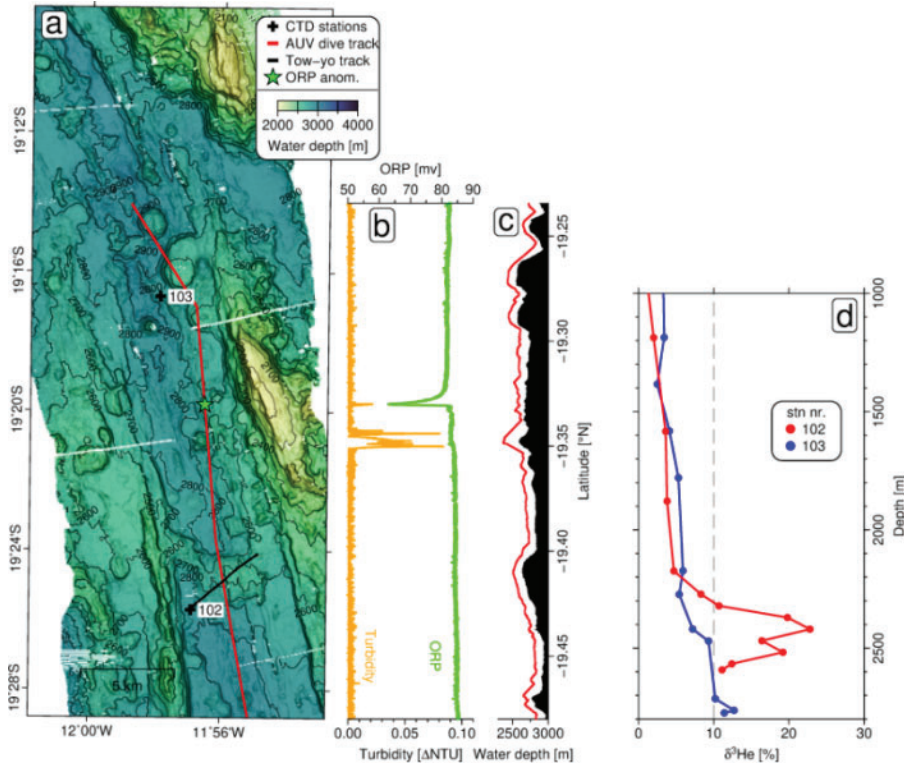


**Figure 7.** Results from the MAR 19° S site. Panel a, bathymetry with AUV track and station locations. Panel b, turbidity and ORP versus latitude along the AUV track plotted in a. Panel c, vehicle and seafloor depths versus latitude along the AUV track. Panel d, vertical profiles of  $\delta^3\text{He}$  for stations 102 and 103.

### 358 5.3.6 MAR 23° S

359 The 22°54' S - 24°24' S segment was surveyed by five vertical CTD casts, one tow-yo and one  
 360 long-range AUV dive, which zigzagged across the axial valley from north to south (Figure 8a). A plume  
 361 was discovered near the start of the AUV mission (Figure 8a). The ridge axis in this region is defined by  
 362 the (to date) southernmost known oceanic core complex (OCC) on the Mid-Atlantic Ridge. This OCC  
 363 exhibits typical ridge-perpendicular corrugations and measures ~16 km along strike. The OCC rises high  
 364 above the surrounding axial valley floor and large rider blocks (or volcanic ridges) sitting on top, mostly  
 365 on its northern part (Figure 8a). The strongest ORP signal was detected on top of the detachment fault  
 366 surface, about 1.5 km east of the hanging-wall cut-off and in proximity to a topographic feature, possibly a  
 367 rider block or volcanic ridge (Figure 8b). Tow-yo station 70 was towed in a W→E direction and the  
 368 MAPR data revealed a particle plume between 2500 and 2700 m depth (Figure 8e) that is coincident with  
 369 ORP anomalies of up to -61 mV near the western end of the tow-yo track (near 23°44.68'S/13°23.59'W)  
 370 indicating the location of the vent field which is ~ 6 km E off the ridge axis (Figure 8a, b). Water samples  
 371 collected ~1 km east of the strongest ORP anomaly show high  $\delta^3\text{He}$  values up to 42.4 % within the  
 372 particle plume (bottles 5,6,8 in Figure 8f).

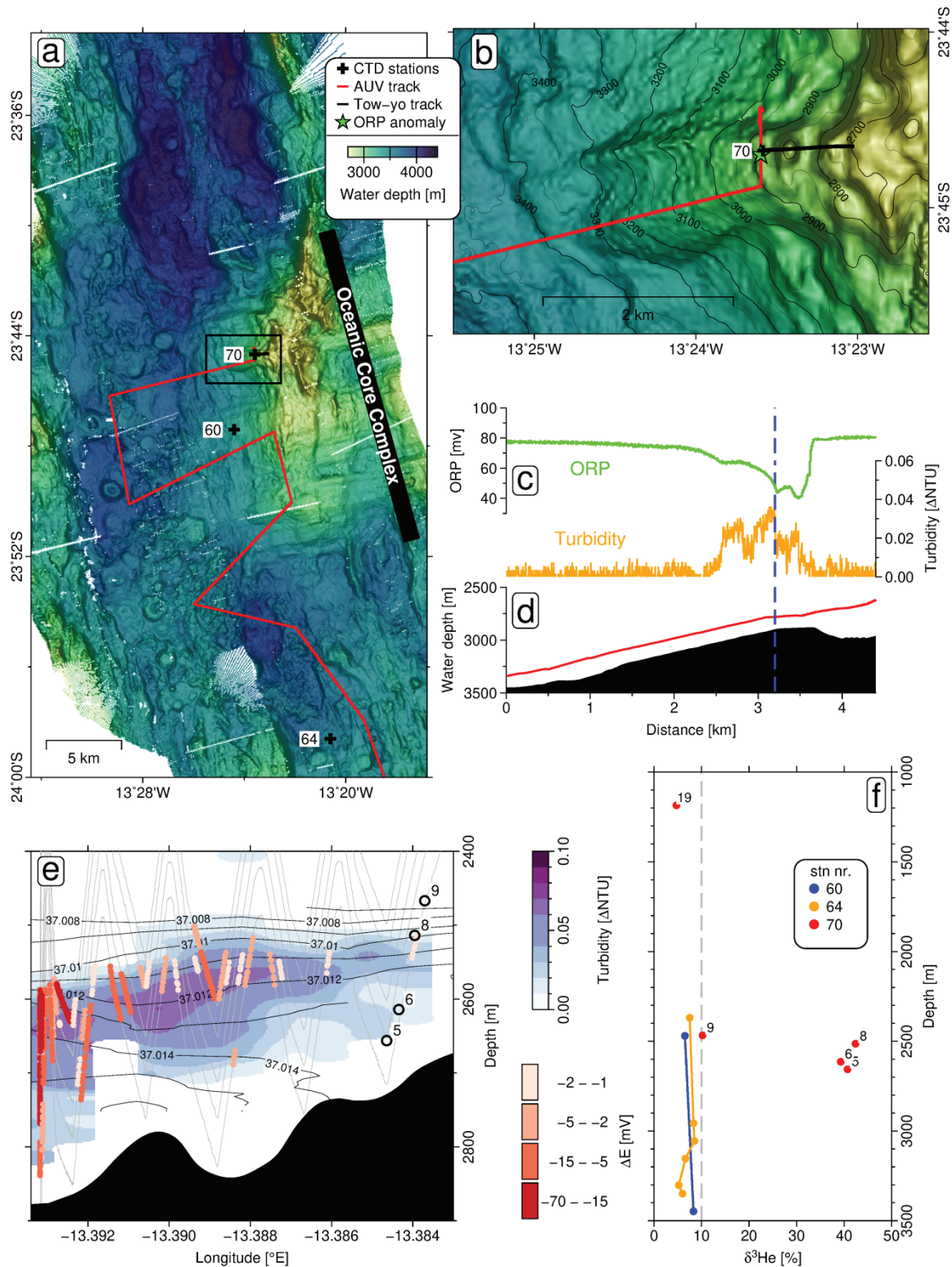


**Figure 8.** Results from the 23°S segment. Map a provides an overview of the ridge segment with black bar roughly indicating the N-S extend of the oceanic core complex. The black frame indicates the perimeter of map b. Map b shows a sub-section of the AUV track in vicinity of the discovered plume. Panel c shows AUV turbidity and ORP data measured along the track section displayed in map b. Panel d indicates the vehicle and seafloor depths along the track section

*displayed in map b. Note, the AUV was diving from north to southwest and the location where heading was altered is indicated by the vertical dashed line. Panel e, results from tow-yo station 70 with faint gray lines indicating MAPR tracks, the blue shading representing turbidity and colored red dots showing ORP anomalies. Numbered circles show water sampling locations and black contours are isopycnals calculated from CTD data. Panel f,  $\delta^3\text{He}$  profiles of stations 60, 64 and 70 with labels corresponding to bottle numbers of station 70 in panel e.*

373                   **5.3.7 MAR 25° S**

374                   The 24°56'S – 25°36'S segment was investigated by two vertical CTD casts (52, 56) and tow-yo  
375 station 54 above the generally smooth-topped axial high at the center of the segment (Figure 9a). ORP  
376 anomalies up to -31 mV were detected in the first 100 m above the seafloor, near the start of the tow-yo  
377 (around 25°20.10'S/13° 37.83'W; Figure 9b, c) indicating the potential vent site location. A weak increase  
378 in turbidity rising ~220 m above the seafloor was detected ~1 km north of the ORP anomalies (Figure 9c).  
379 No turbidity or ORP anomalies were detected on the W→E trending portion of the tow-yo cast and the  
380  $\delta^3\text{He}$  values from the western end of the tow-yo station, did not exceed the oceanic background (Figure  
381 9d). Since the water samples stem from distances further than 4 km from the ORP signal, it cannot be  
382 ruled out that this vent site discharges minor amounts of  $^3\text{He}$ .

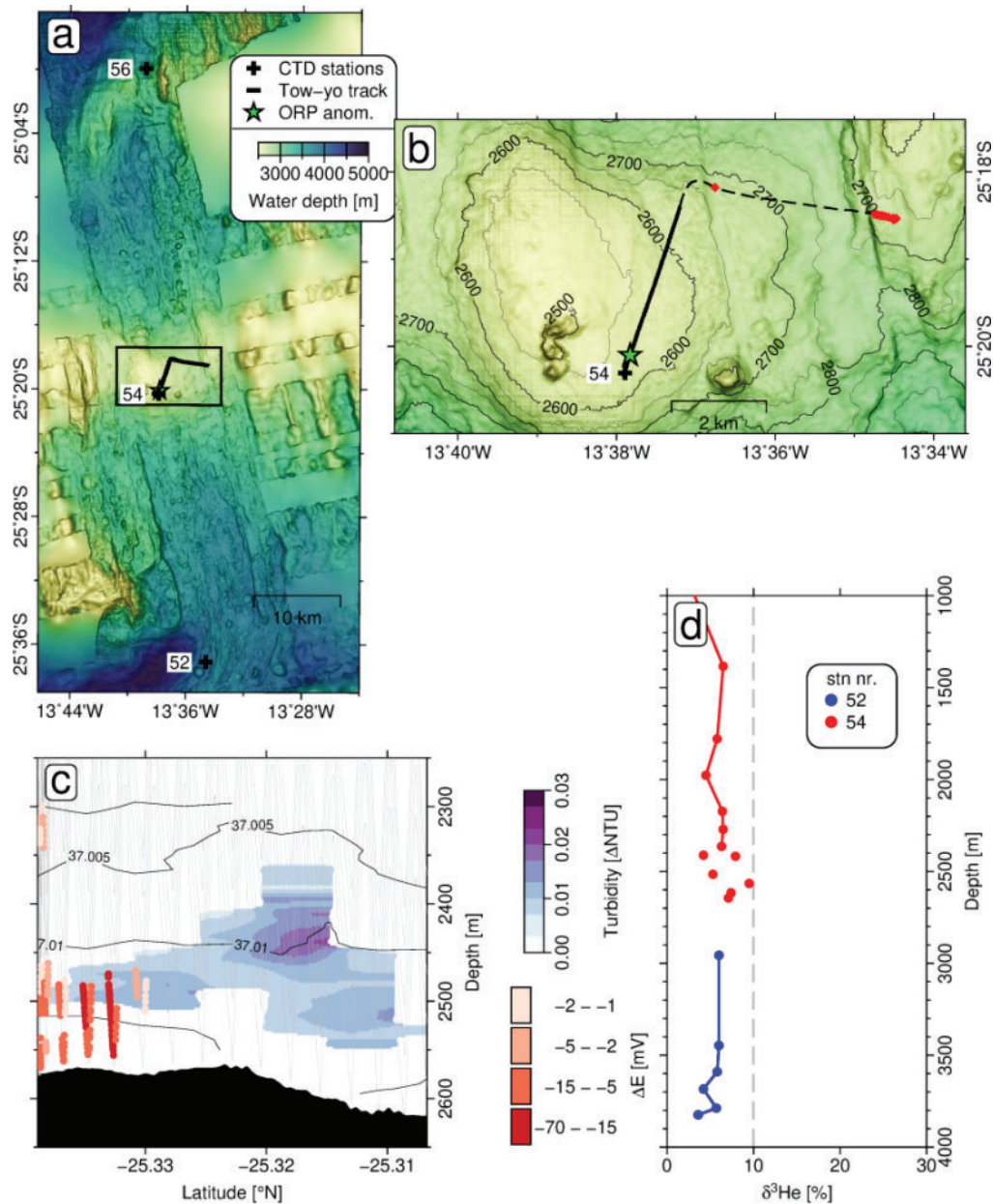


**Figure 9.** Results from the 25°S plume site. Map a, bathymetry of the ridge segment with the black frame indicating the perimeter of map b. Red diamonds on map b indicate locations of water sampling, used for helium analysis. Panel c, results from the S→N trending portion of tow-yo station 54 (track shown on map b) with blue shading representing turbidity and red dots showing  $\Delta E$  anomalies. Panel d,  $\delta^3\text{He}$  profiles of stations 52 and 54.

383

384

### 5.3.8 Merian Vent Field (26°S)

385 The 25°42'S – 26°36'S segment was investigated by three vertical CTD casts, one tow-yo and one  
 386 AUV dive (Figure 10). A turbidity plume rising ~280 m above the seafloor and strong ORP anomalies  
 387 were discovered during tow-yo 48 traversing the axial high at 26°S of which the shallowest part is cross-  
 388 cut by a series of ridge-parallel fault scarps (Figure 10a, c). The plume discovery motivated a dedicated  
 389 AUV mission of densely spaced survey lines flown at 50 m altitude above the axial high (Figure 10a, b).

390 The AUV and tow-yo turbidity data agree in the location of the densest particle cloud, above the center of  
391 the axial high (Figure 10b,c). The AUV detected an ORP anomaly of  $\Delta E = -19$  mV, coincident with a  
392  $+0.05$  °C temperature spike, at  $26^{\circ}0.99'S/13^{\circ}51.17'W$  originating from the nearby Merian Vent Field,  
393 discovered during the MSM-25 cruise (green circle in Figure 10c; Devey and cruise-participants, 2013).  
394 Another ORP anomaly of  $\Delta E = -43$  mV, paralleled by a  $+0.03$  °C temperature anomaly, was detected at  
395  $26^{\circ}2.71'S/13^{\circ}50.88'W$  (marked as Site II in Figure 10a-c) that is not accompanied by a particle plume.

396 Water samples collected during tow-yo 48 yield a  $\delta^3\text{He}$  maximum of 52.2 % in the center of the  
397 particle plume (bottle number 7; Figure 10c, d). Water samples from station 51 (Figure 10a, e) show  
398 increased  $\delta^3\text{He}$  values of up to 16.0 % at 3815 m depth (~20 m above the seafloor) which are likely  
399 unrelated to the plume above the axial high and suggest another undiscovered vent at the segment's  
400 southern end. Near-bottom current velocities above the axial high average around  $12\text{ cm s}^{-1}$ , with  
401 directions between NW and SW (Figure 10c). Predicted barotropic tidal currents average around  $5\text{ cm s}^{-1}$   
402 and their directions evolve from NW to S over the course of the two-yo station (Figure 10c) suggesting  
403 that bottom currents above the axial high are not fully in phase with barotropic tides and a residual flow of  
404 westerly direction prevails.

405 The identified ORP anomalies suggest there is one further active hydrothermal field on the axial  
406 high besides the Merian Vent Field (Site II; Figure 10a-c), following the definition of Baker et al. (2016)  
407 who consider venting sites separated more than 1 km as individual vent fields. The dense particle plume  
408 above axial high is likely created by the Merian Vent Field and dispersed by the W directed residual  
409 bottom currents. The absence of turbidity plumes above venting sites II and III could either be attributed  
410 to sparse sampling (flying at 50 m altitude, the AUV might have passed below such plumes) or a different,  
411 particle-poor type of venting.

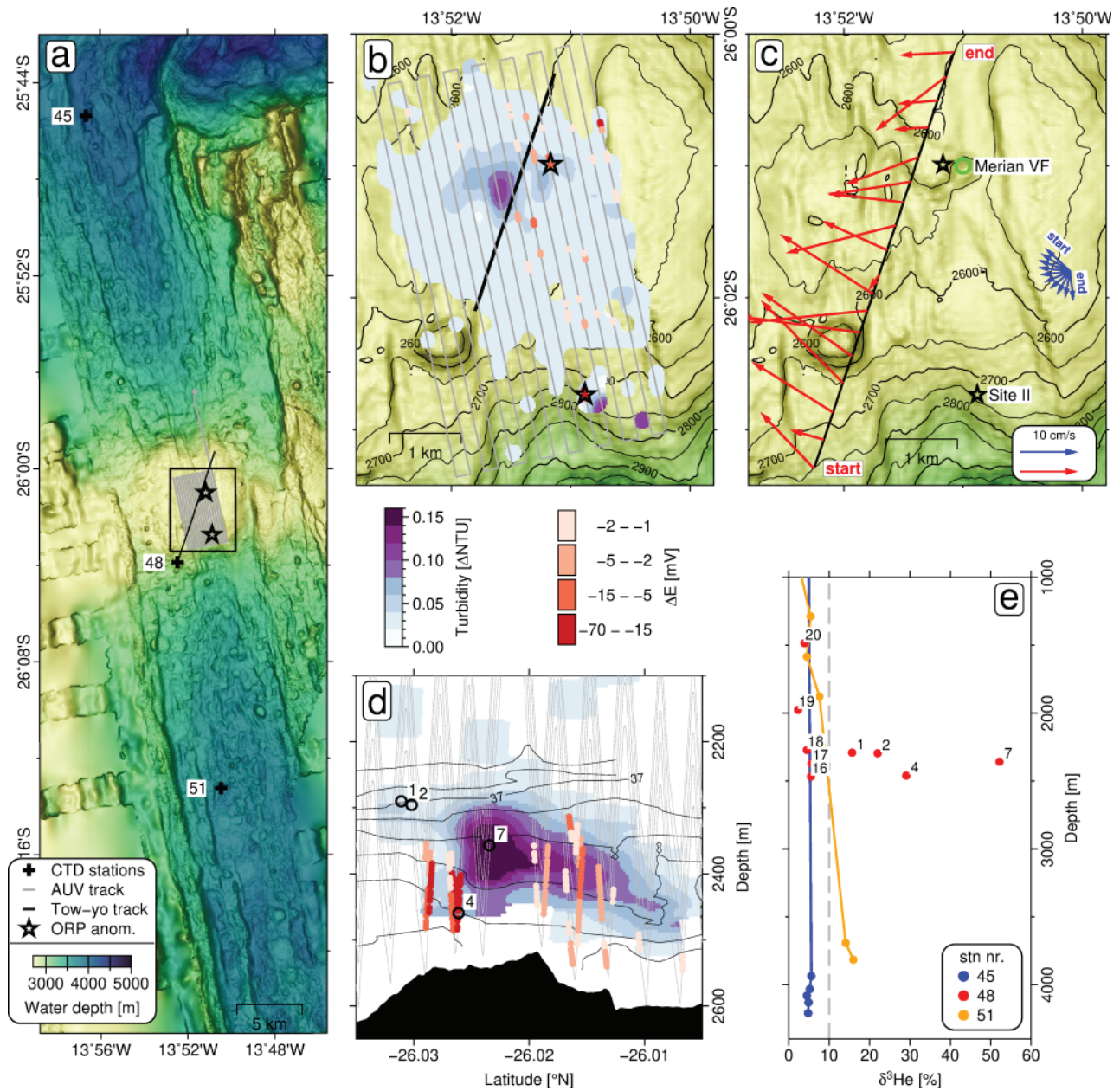


**Figure 10.** Results from the 25°42'S – 26°36'S segment. Map a gives an overview of the segment and the perimeter of maps b,c (black frame). Map b shows the AUV track (gray lines) and tow-yo track (black line). Blue shading, AUV turbidity data colored at the same scale as MAPR data in panel d and red dots  $\Delta E$  anomalies at the same color scale as MAPR data in panel d. Note, the AUV was flown at 50 m above seafloor and remained below the center of the turbidity plume. Map c, red vectors show average measured current velocities in the lowermost 200 m and blue arrows show predicted barotropic tidal current velocities. Green circle indicates the location of the Merian Vent Field (Devey and cruise-participants, 2013). Panel d, results from tow-yo 48 track plotted in c. Faint gray lines indicating MAPR tracks, blue shading representing turbidity and red dots showing  $\Delta E$  anomalies (color bars above). Numbered circles show water sampling locations and black contours are isopycnals. Panel e,  $\delta^3\text{He}$  profiles 45, 48 and 51 with labels corresponding to bottle numbers of station 48 in panel d.

412

### 5.3.9 MAR 2640'S – 27°50'S

413

414

415

416

417

418

419

420

In the 26°40'S – 27°50'S region was investigated by one AUV dive and four vertical CTD casts (Figure 11a). The AUV detected two ORP anomalies at 27° 8.86'S/13°28.52'W ( $\Delta E = -10$  mV) and at 27° 47.62'S/13°22.38'W ( $\Delta E = -30$  mV). The northern anomaly is accompanied by a 0.03  $\Delta$ NTU turbidity increase (Figure 11b). None of the water samples collected along the AUV track showed increased  $^3\text{He}$  concentrations (Figure 11d). Three water samples collected at station 42 (at 26°42.58'S/13°36.59'W) in water depths of 3250 - 3350 m yield  $\delta^3\text{He}$  values of 16.8 – 18.0 %. This  $^3\text{He}$  plume did not coincide with any turbidity or ORP anomalies but has a considerable rise height of ~500 m above the seafloor and suggests active hydrothermal venting in the vicinity of station 42.

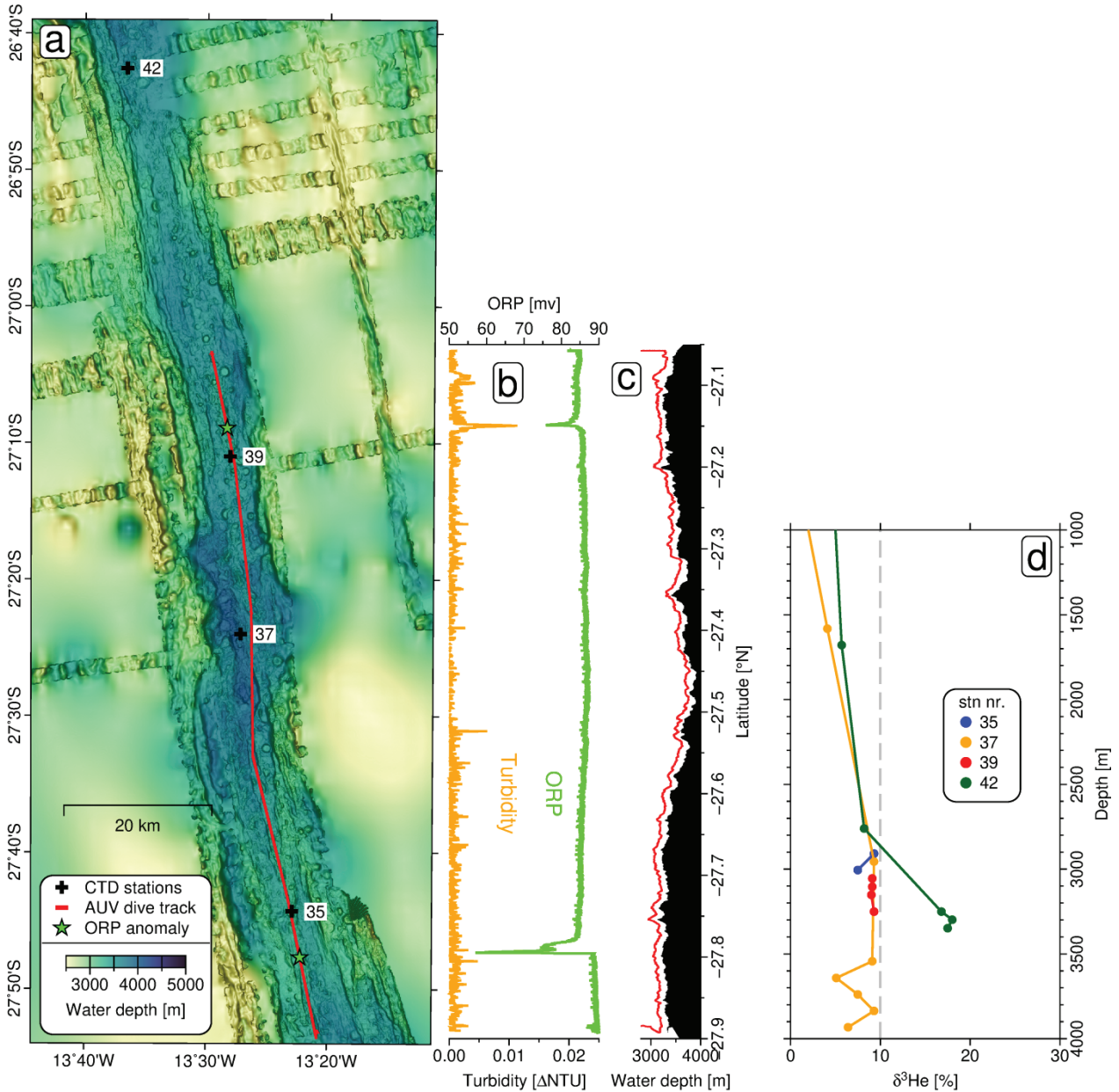


**Figure 11.** Results from the 26°40'S – 27°50'S region. Map a, bathymetry of the ridge segment with AUV track and CTD stations. Panel b, turbidity and ORP versus latitude along the AUV track. Panel c, vehicle- and seafloor depth versus latitude along the AUV track. Panel d, vertical profiles of  $\delta^3\text{He}$  for stations 35, 37, 39 and 42.

421

### 5.3.10 MAR 30°50'S

422

423

424

425

426

Vertical CTD 19 station was placed at the center of the ridge segment between 30°38'S and 31°13'S (Figure 12a). One water sample at 2809 m depth yielded a  $\delta^3\text{He}$  value of 12.8 % and the MAPR detected an ORP anomaly between 2805 – 2940 m depth, i.e. ~400 m above the seafloor (Figure 12b) but no coincident turbidity anomaly was detected. Although weak, we infer our findings give evidence for hydrothermal activity in the vicinity of station 19.

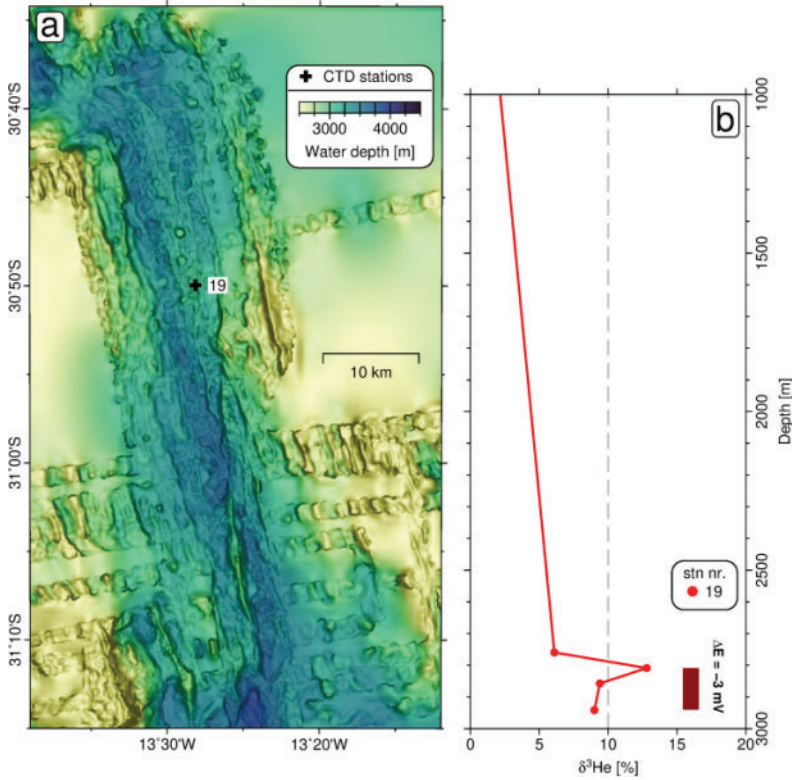


**Figure 12.** Results from the 30°50'S plume site. Map a, bathymetry of the ridge segment. Panel b shows  $\delta^3\text{He}$  results and the depth of an ORP anomaly at station 19.

427

### 5.3.11 MAR 31°40'S

428

429

430

431

432

433

434

435

436

437

438

439

The 30°15'S - 32°5'S segment was investigated by one long-range AUV dive and five vertical CTD casts (Figure 14a). A turbidity anomaly of 0.007  $\Delta\text{NTU}$  was found at 31°44.26'S/13°22.63'W in 2890 m water depth above an axial high at the segments center (Figure 13b, c). Since no ORP data is available from this AUV dive a coincident ORP anomaly cannot be confirmed. Water samples collected at station 14 (~3 km south of the turbidity anomaly) did not show an increase in  $^3\text{He}$  but a slightly increased  $\delta^3\text{He}$  value of 10.7 % was found at 3955 m depth at station 16 (Figure 13d) approximately 23 km north of the AUV turbidity anomaly. While it seems likely that there is hydrothermal activity at this ridge segment, we can only speculate about the vent location and whether the  $^3\text{He}$  signal at station 16 and the turbidity plume above the segment center have a common source or not. The increased  $\delta^3\text{He}$  value of 11.4 % at 3660 m depth (70 m above the seafloor) sampled at station 12 near the southern end of the segment seems too deep to originate from within the segment and may stem from an unknown source in the fracture zone (Figure 13a, d).

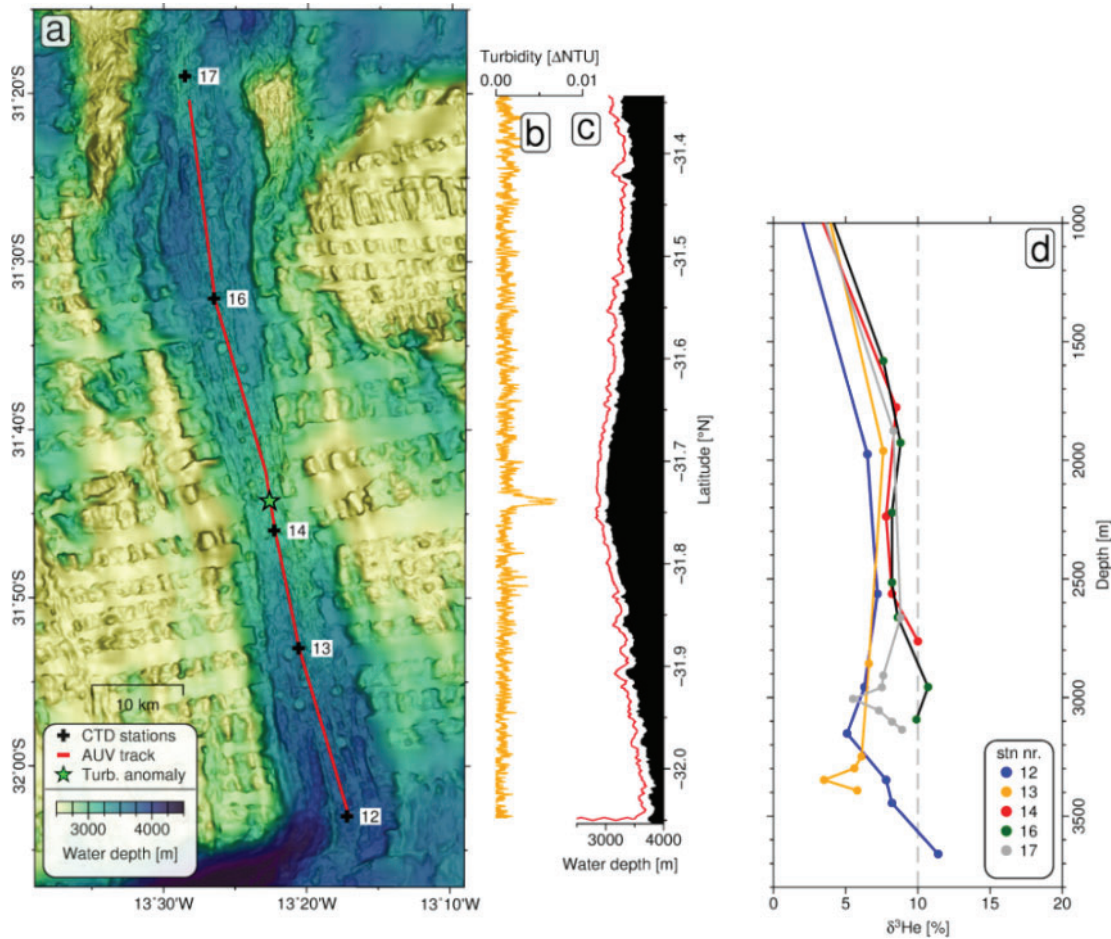


**Figure 13.** Map a gives an overview of the ridge segment, AUV track and CTD stations. Panel b, turbidity versus latitude along the AUV track. No ORP data is available from this dive. Panel c, vehicle- and seafloor depth versus latitude along the AUV track. Panel d, vertical profiles  $\delta^3\text{He}$  for stations 12 – 17.

#### 440 5.3.12 MAR 33°S

441 The most southerly segment investigated (32°30'S-33°30'S) was surveyed by a long-range AUV  
 442 mission, one tow-yo (6) and three vertical CTD casts (3, 5, 7; Figure 14a). The segment center is  
 443 characterized by an axial volcanic high at which the seafloor is covered by numerous mounds of variable  
 444 size (Figure 15a, b). During the AUV mission two distinct ORP anomalies were detected at  
 445 32°58.06'S/14°27.10'W ( $\Delta E = -72$  mV; Site I) and at 32°59.68'S/14°26.55'W ( $\Delta E_h = -32$  mV; Site II)  
 446 that are marked by stars in Figure 14a, b. The ORP anomaly at Site I consists of three consecutive pulses  
 447 within a strike distance of 650 m and the AUV CTD data revealed a +0.03°C spike in temperature  
 448 coincident with the strongest ORP anomaly (Figure 14c). Sites I and II are associated with turbidity  
 449 plumes and additional turbidity anomalies were found ~2 km and ~6 km north of Site I (Figure 14c). No  
 450 turbidity or ORP signal was detected along tow-yo 6 (Figure 14a) but a  $\delta^3\text{He}$  value of 18.2 % was found at  
 451 2367 m water depth near the northern end of tow-yo 6 (Figure 14e). The three repeated ORP pluses and  
 452 the temperature spike at Site I indicate a field of multiple active chimneys. The ORP, temperature and  
 453 turbidity anomalies at Site II indicate another active vent field.

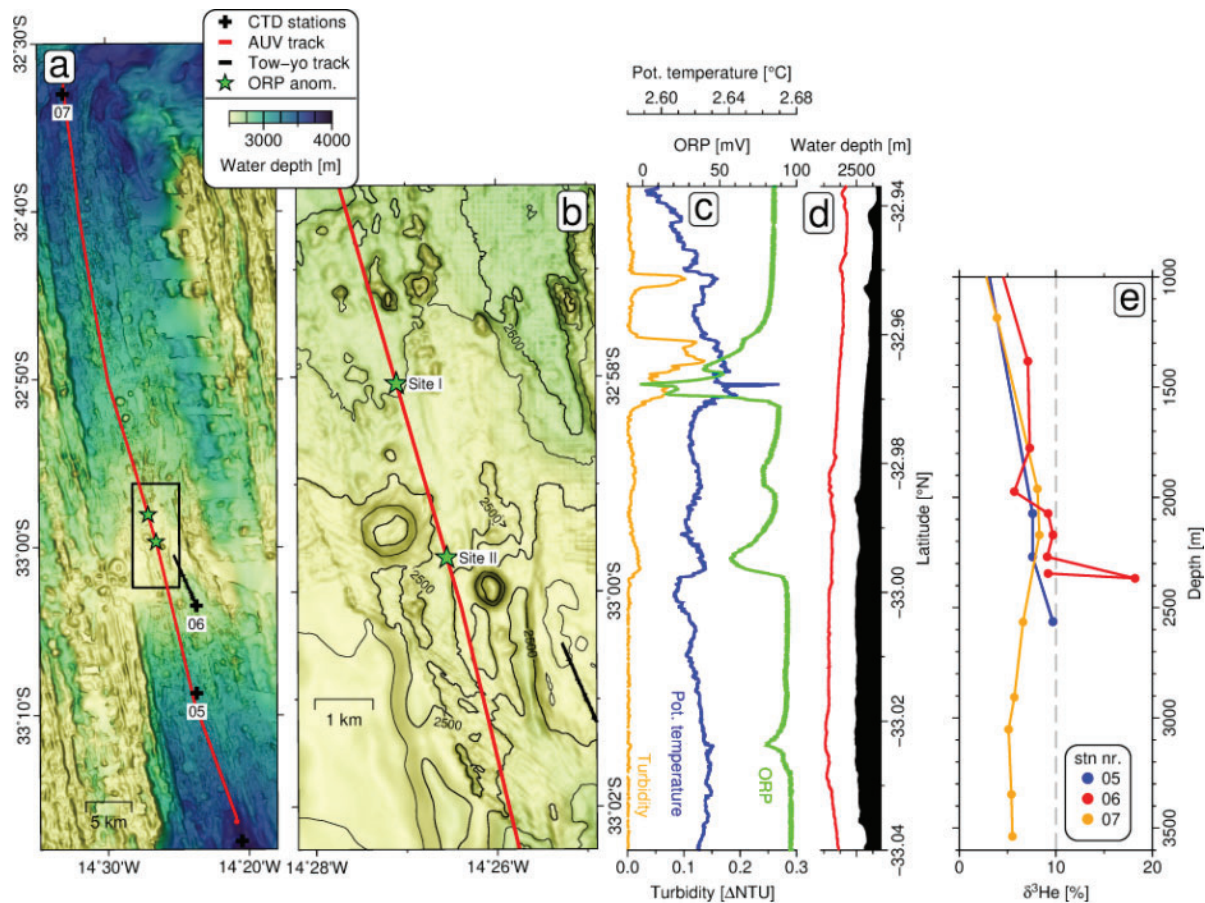
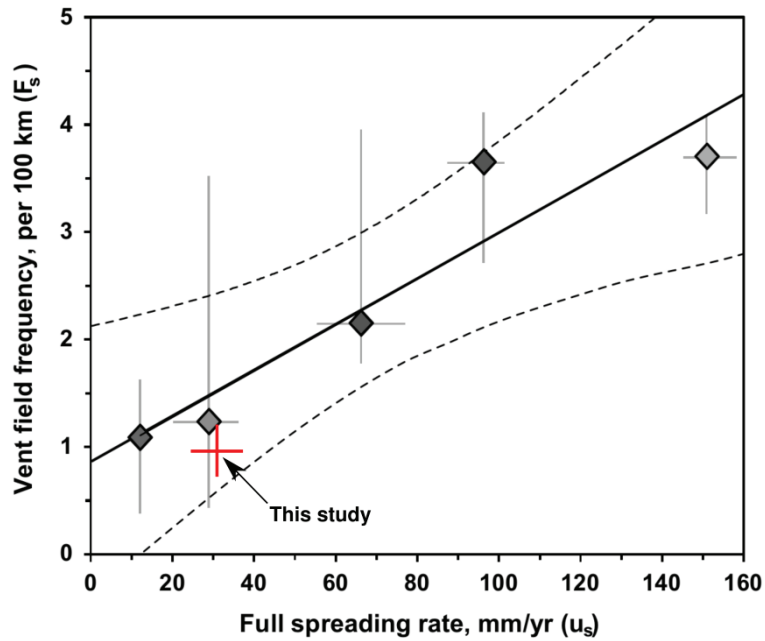


**Figure 14.** Results from the 33°S axial high. Map a, bathymetry of the ridge segment with black frame indicating perimeter of map b. Panel c, turbidity, potential temperature and ORP versus latitude along the AUV track displayed on map b. Panel d, vehicle- and seafloor depth versus latitude along the AUV track. Panel e, vertical profiles of  $\delta^3\text{He}$  for stations 5 – 7. Note, that no turbidity or ORP anomaly was detected at tow-yo station 6.

#### 454 5.4 Relation to Vent Field Frequency along the Global MORs

455 Our survey covered approximately 2100 km of the SMAR axis (excluding transforms) along  
 456 which hydrothermal plumes were found at ten ridge segments, providing the location of 14 new and three  
 457 previously known hydrothermal vent fields. A summary of all confirmed and inferred sites is given in  
 458 Table 1, including the previously known Zouyu-1 and Rainbow Bay vent fields (Tao et al., 2011; Tao et  
 459 al., 2017) that have not been visited during the MSM-25 cruise. We count a total number of 19 vent fields  
 460 in the 13°-33°S region implying an average vent field incidence of 0.9 vent fields per 100 km ridge axis.  
 461 With spreading rates of 32-34 mm yr<sup>-1</sup> in this region the inferred frequency matches well with the latest  
 462 global compilations of vent field incidence (Beaulieu et al., 2015; Hannington et al., 2011; Figure 15).



463

464 **Figure 15.** Relation of the vent field frequency in the 13°-33°S region of the SMAR to the vent  
 465 field frequency along the global Mid-Ocean Ridges (from the compilation of Beaulieu et al., (2015)).  
 466 Diamonds represent hydrothermal survey results from non-hotspot influenced ridges binned into five  
 467 spreading rate categories. Horizontal and vertical bars show give the range of data points for each  
 468 category. Figure is from Beaulieu et al., (2015).

469 The actual number of vent fields in the 13°-33° region may even be higher, assuming our survey  
 470 has missed odd sites. Sampling even in close proximity to active vents does not always return a plume  
 471 signal, as demonstrated in the case of station 113 at ~1.5 km distance to the Deyin-1 vent site where no  
 472 plume signal was found by our vertical CTD cast (Figure 5). Thus, our number of inferred vent fields may  
 473 be considered a minimum estimate. Since the AUV dives and CTD stations focused on the center of the  
 474 axial valley, we would also have not detected any off-axis systems, with the exception of the 23°S  
 475 segment, where the off-axis core complex was specifically targeted with the AUV.  
 476

**Table 1.** Summary of all confirmed and inferred hydrothermal venting sites in the 13°-33°S region.

(Prelim.) site name	Seg. surveyed during MSM-25	Inferred vent field locations	Max turbidity [ $\Delta$ NTU]	Max $\Delta$ E [mV]	Max. $\delta^3\text{He}$ [‰]	Approx. seafloor depth of vent [m]	Approx. rise height of plume [m]	Tectonic setting	MSM-25 CTD stations	MSM-25 AUV dive
Zouyu-1 <sup>a</sup>	16	13°15.0'S/14°24.6'W <sup>a</sup>	-	-	-	2300	unknown	Axial high	-	-
Zouyu-2	16	13°17.31'S/14°24.59'W <sup>c</sup>	0.14 (MAPR)	-56 (MAPR)	146.9	2300	200	Axial high	124	#135
Tai Chi	16	13°35.41'S/14°31.21'W <sup>e</sup>	0.19 (MAPR)	-83 (MAPR)	29.5	3180	380	At eastern valley wall	122	-
Rainbow Bay <sup>b</sup>	16	14°3.6'S/14°20.4'W <sup>b</sup>	-	-	-	2900	unknown	At eastern valley wall	-	-
Deyin-1	15	15°9.97'S/13°21.34'W <sup>d</sup>	0.06 (MAPR)	-20 (MAPR)	25.9	2850	350	Center of axial valley	116	#134
MAR 17°S	14	17°15.13'S/14°13.62'W <sup>e</sup>	0.008 (MAPR)	-21 (MAPR)	19.9	3280	280	Axial high	107	-
MAR 19°S	12	19°19.81'S/11°56.53'W <sup>d</sup>	0.08 (AUV)	-22 (AUV)	22.8	2700	unknown	At valley bottom	102	#133
MAR 23°S	9	23°44.7'S/13°23.6'W <sup>d</sup>	0.08 (MAPR)	-61 (MAPR)	42.4	2880	350	on top of oceanic core complex	070	#129
MAR 25°S	8	25°20.10'S/13°37.83'W <sup>d</sup>	0.02 (MAPR)	-31 (MAPR)	none?	2570	200	Axial high	054	-
Merian Vent Field	7	26°00.99'S/13°51.17'W <sup>d</sup>	0.15 (MAPR)	-19 (AUV)	52.2	2550	280	Axial high	048	#128
	7	26°02.71'S/13°50.88'W <sup>d</sup>	unknown	-43 (AUV)	unknown	2750	unknown	Axial high	048	#128
MAR 26.2°S	7	26°13.24'S/13°50.47'W <sup>d</sup>	unknown	unknown	16.0	3825	unkown	unkown	051	-
MAR 26.7°S	7	26°42.58'S/13°36.59'W <sup>d</sup>	unknown	unknown	18.0	2400	500	unkown	042	-
MAR 27°S	6	27°8.86'S/13°28.52'W <sup>d</sup>	0.03 (AUV)	-10 (AUV)	unknown	3400	unknown	At valley bottom	039	#127
MAR 28°S	6	27°47.62'S/13°22.38'W <sup>d</sup>	none	-30 (AUV)	unknown	3100	unknown	Center of axial valley	035	#127
MAR 30.8°S	2	30°49.96'S/13°28.14'W <sup>e</sup>	none	-3 (MAPR)	12.8	2950	180	Center of axial valley	019	-
MAR 31°S	2	31°44.26'S/13°22.63'W <sup>f</sup>	0.007 (AUV)	unknown	unknown	3050	unknown	Axial high	Near 014	#125
MAR 33°S	1	32°58.06'S/14°27.10'W <sup>d</sup>	0.13 (AUV)	-72 (AUV)	unknown	2600	unknown	Axial high		#124
	1	32°59.68'S/14°26.55'W <sup>d</sup>	0.07 (AUV)	-32 (AUV)	unknown	2600	unknown	Axial high		#124

477 <sup>a</sup>location from *Tao et al.* (2017). <sup>b</sup>location from *Tao et al.* (2011). <sup>c</sup>location of buoyant plume. <sup>d</sup>location of strong  
478 ORP anomaly. <sup>e</sup>location of CTD station detecting plume signal. <sup>f</sup>location of turbidity anomaly. Note, the Zouyu-1  
479 and Rainbow Bay sites have not been visited during our study but are listed here for completeness.  
480

## 481 6 Conclusions

482 Knowing the seafloor location of active venting sites is a crucial prerequisite for the later planning  
483 of detailed studies on hydrothermal activity, biogeographical distribution of endemic vent fauna, and of  
484 seafloor massive sulfide deposits along MORs. We present the results of an over 2100 km-long systematic

485 plume survey in the 13°S-33°S region of the SMAR, a previously virtually unexplored ridge region.  
486 During expedition MSM-25 we identified previously unknown plumes above ten ridge segments and  
487 confirmed three previously known hydrothermal plumes using a combination of three independent  
488 hydrothermal tracers: ORP, turbidity and <sup>3</sup>He. The major advantage of combining these tracers is their  
489 independence and difference in behavior. ORP is best for the near field, turbidity is easiest to detect and  
490 <sup>3</sup>He is a fully conservative tracer. Upon careful evaluation of the plume data we were able to infer the  
491 approximate seafloor locations of 14 previously unknown and three known vent fields in the 13°S-33°S  
492 region. A majority of the explored sites are associated with morphologically pronounced axial volcanic  
493 highs, suggesting a close relationship between hydrothermalism and magmatism in this region. An  
494 exception is the inferred vent field at 23°S, located ~6 km off-axis, on top of the southernmost known  
495 oceanic core complex on the Mid-Atlantic Ridge.

496 A very unusual hydrothermal plume was observed above the extensive Zouyu Ridge axial  
497 volcanic high at 13°S. Redox anomalies are typically associated with low temperature venting and rise to  
498 lesser heights above the seafloor than particle plumes. A reverse vertical zonation was observed here,  
499 where an extended redox plume occurs ~50 m above the core of a particle plume. This may result from  
500 vertical age stratification in the plume (youngest at top, oldest at bottom) or the presence of two separate  
501 vents feeding the plume, one providing the particles, the other the reduced waters.

502 The average vent field frequency of 0.9 vents per 100 km ridge axis in the 13°-33°S region  
503 matches the vent field frequency predicted by global compilations of vent field incidence versus spreading  
504 rate. We conclude that the results from this reconnaissance study present a comprehensive overview of the  
505 locations of hydrothermal activity in the 13°S-33°S region of the SMAR.

506 The hydrography and absence of vent sites near the Rio de Janeiro Transform, cross-cutting the  
507 SMAR at 22°S, suggests that this region represents a physical barrier to the meridional dispersal of  
508 hydrothermal larvae and possibly constitutes the biogeographic boundary between the different vent fauna  
509 communities found in the North Atlantic and those at the Antarctic Ridges.

510

## 511 Acknowledgments and Availability of Data

512 We acknowledge the captain and crew of RV Maria S. Merian expedition MSM-25. We are especially  
513 grateful to the GEOMAR AUV team and all other scientists of expedition MSM-25 for their contributions  
514 at sea. M. P. thanks O. Huhn for helpful advice on noble gas related matters. All data presented in this  
515 paper will be available via the PANGAEA earth data publisher (<https://pangaea.de>) once the manuscript  
516 has been accepted for publication. MAPRs were kindly provided by the NOAA vents program and the  
517 ORP sensor for the AUV was kindly provided by Ko-ichi Nakamura (AIST, Japan). We acknowledge the  
518 inputs of two anonymous reviewers. Figures were created with the GMT software (Wessel et al., 2013). F.  
519 S. was funded through the DFG Cluster of Excellence ‘*Der Ozean im Erdsystem*’ at the University of  
520 Bremen, grant no. 49926684. M.W. was supported by DFG grant WA 2556/4. This is PMEL contribution  
521 4920.

522

523

## References

524

- 525 Baker, E. T. (2017), Exploring the ocean for hydrothermal venting: New techniques, new discoveries, new  
526 insights, *Ore Geology Reviews*, 86, 55-69, doi: 10.1016/j.oregeorev.2017.02.006.
- 527 Baker, E. T., and C. R. German (2004), On the Global Distribution of Hydrothermal Vent Fields, edited  
528 by C. R. German, J. Lin and L. M. Parson, pp. 245-266, American Geophysical Union.
- 529 Baker, E. T., Y. J. Chen, J. Phipps Morgan, and J. P. Morgan (1996), The relationship between near-axis  
530 hydrothermal cooling and the spreading rate of mid-ocean ridges, *Earth Planet. Sci. Lett.*, 142, 137-145,  
531 doi: 10.1016/0012-821X(96)00097-0.
- 532 Baker, E. T., M.-H. Cormier, C. H. Langmuir, and K. Zavala (2001), Hydrothermal plumes along  
533 segments of contrasting magmatic influence, 15°20'-18°30'N, East Pacific Rise, *Geochemistry,  
534 Geophysics, Geosystems*, 2(9), doi: 10.1029/2000GC000165.
- 535 Baker, E. T., J. A. Resing, R. M. Haymon, V. Tunnicliffe, J. W. Lavelle, F. Martinez, V. Ferrini, S. L.  
536 Walker, and K. Nakamura (2016), How many vent fields? New estimates of vent field populations on  
537 ocean ridges from precise mapping of hydrothermal discharge locations, *Earth and Planetary Science  
538 Letters*, 449, 186-196, doi: 10.1016/j.epsl.2016.05.031.
- 539 Baker, E. T., S. L. Walker, J. A. Resing, W. W. Chadwick, S. G. Merle, M. O. Anderson, D. A.  
540 Butterfield, N. J. Buck, and S. Michael (2017), The Effect of Arc Proximity on Hydrothermal Activity  
541 Along Spreading Centers, *Geochemistry, Geophysics, Geosystems*, 18(11), 4211-4228, doi:  
542 10.1002/2017GC007234.
- 543 Beaulieu, S. E. (2015), InterRidge Global Database of Active Submarine Hydrothermal Vent Fields:  
544 prepared for InterRidge, Version 3.4, World Wide Web electronic publication, accessed 2018-06-22.
- 545 Beaulieu, S. E., E. T. Baker, and C. R. German (2015), Where are the undiscovered hydrothermal vents on  
546 oceanic spreading ridges?, *Deep Sea Research Part II: Topical Studies in Oceanography*, 121, 202-212,  
547 doi: 10.1016/j.dsr2.2015.05.001.
- 548 Beaulieu, S. E., E. T. Baker, C. R. German, and A. Maffei (2013), An authoritative global database for  
549 active submarine hydrothermal vent fields, *Geochemistry, Geophysics, Geosystems*, 14(11), 4892-4905,  
550 doi: 10.1002/2013GC004998.
- 551 Broecker, W. S., T. Takahashi, and Y. H. Li (1976), Hydrography of the central Atlantic—I. The two-  
552 degree discontinuity, *Deep Sea Research and Oceanographic Abstracts*, 23(April), 1083-1104, doi:  
553 10.1016/0011-7471(76)90886-X.
- 554 Charlou, J. L., Y. Fouquet, H. Bougault, J. P. Donval, J. Etoubleau, P. Jean-Baptiste, A. Dapigny, P.  
555 Appriou, and P. A. Rona (1998), Intense CH<sub>4</sub> plumes generated by serpentinization of ultramafic rocks at  
556 the intersection of the 15°20'N fracture zone and the Mid-Atlantic Ridge, *Geochimica et Cosmochimica  
557 Acta*, 62, 2323-2333, doi: 10.1016/S0016-7037(98)00138-0.
- 558 Copley, J. T., et al. (2016), Ecology and biogeography of megafauna and macrofauna at the first known  
559 deep-sea hydrothermal vents on the ultraslow-spreading Southwest Indian Ridge, *Scientific Reports*, 6,  
560 39158, doi: 10.1038/srep39158.

561 Corliss, J. B., et al. (1979), Submarine Thermal Springs on the Galapagos Rift, *Science*, 203(4385), 1073-  
562 1083, doi: 10.1126/science.203.4385.1073.

563 DeMets, C., R. G. Gordon, and D. F. Argus (2010), Geologically current plate motions, *Geophys. J. Int.*,  
564 181, 1-80, doi: 10.1111/j.1365-246X.2009.04491.x.

565 Devey, C. W., and cruise-participants (2013), SoMARTerm: The Mid-Atlantic Ridge 13-33°S, *Maria S.*  
566 *Merian Berichte*, doi: 10.2312/cr\_msm25.

567 Devey, C. W., C. R. German, K. M. Haase, K. S. Lackschewitz, B. Melchert, and D. P. Connelly (2010),  
568 The relationships between volcanism, tectonism and hydrothermal activity on the Mid-Atlantic Ridge  
569 south of the equator, in *Diversity of hydrothermal systems on slow spreading ocean ridges*, edited, pp.  
570 133-152.

571 Edmond, J. M., C. Measures, R. E. McDuff, L. H. Chan, R. Collier, B. Grant, L. I. Gordon, and J. B.  
572 Corliss (1979), Ridge crest hydrothermal activity and the balances of the major and minor elements in the  
573 ocean: The Galapagos data, *Earth and Planetary Science Letters*, 46(1), 1-18, doi: 10.1016/0012-  
574 821X(79)90061-X.

575 Edmonds, H. N. (2010), Chemical Signatures From Hydrothermal Venting on Slow Spreading Ridges, in  
576 *Diversity of Hydrothermal Systems on Slow Spreading Ocean Ridges*, edited, pp. 27-42.

577 Egbert, G. D., and S. Y. Erofeeva (2002), Efficient Inverse Modeling of Barotropic Ocean Tides, *Journal*  
578 *of Atmosphere and Ocean Technology*, 19, 183-204, doi: 10.1175/1520-0426(2002)019.

579 Elderfield, H., and A. Schultz (1996), Mid-Ocean Ridge Hydrothermal Fluxes and the Chemical  
580 Composition of the Ocean, *Annual Review of Earth and Planetary Sciences*, 24(1), 191-224, doi:  
581 10.1146/annurev.earth.24.1.191.

582 Feely, R. A., G. J. Massoth, J. H. Trefry, T. Baker, J. Paulson, and T. Lebon (1994), Composition and  
583 sedimentation of hydrothermal plume particles from North Cleft segment , Juan de Fuca Ridge, *Journal of*  
584 *Geophysical Research: Oceans*, 99(B3), 4985-5006, doi: 10.1029/93JB02509.

585 Fisher, C., K. Takai, and N. Le Bris (2007), Hydrothermal Vent Ecosystems, *Oceanography*, 20(1), 14-23,  
586 doi: 10.5670/oceanog.2007.75.

587 Fouquet, Y., et al. (2010), Geodiversity of hydrothermal processes along the mid-atlantic ridge and  
588 ultramafic-hosted mineralization: A new type of oceanic Cu-Zn-Co-Au volcanogenic massive sulfide  
589 deposit, in *Geophysical Monograph Series*, edited, pp. 321-367.

590 German, C. R., and L. M. Parson (1998), Distributions of hydrothermal activity along the Mid-Atlantic  
591 Ridge : interplay of magmatic and tectonic controls, *Earth and Planetary Science Letters*, 160, 327-341.

592 German, C. R., S. Petersen, and M. D. Hannington (2016), Hydrothermal exploration of mid-ocean ridges:  
593 Where might the largest sulfide deposits be forming?, *Chemical Geology*, 420, 114-126, doi:  
594 10.1016/j.chemgeo.2015.11.006.

595 Haase, K. M., et al. (2007), Young volcanism and related hydrothermal activity at 5°S on the slow-  
596 spreading southern Mid-Atlantic Ridge, *Geochemistry, Geophysics, Geosystems*, 8, doi:  
597 10.1029/2006gc001509.

598 Hannington, M. D., J. Jamieson, T. Monecke, S. Petersen, and S. E. Beaulieu (2011), The abundance of  
599 seafloor massive sulfide deposits, *Geology*, 39(12), 1155-1158, doi: 10.1130/G32468.1.

600 Hasterok, D. (2013), A heat flow based cooling model for tectonic plates, *Earth and Planetary Science*  
601 *Letters*, 361, 34-43, doi: 10.1016/j.epsl.2012.10.036.

602 Jean-Baptiste, P., E. Fourré, J. L. Charlou, C. R. German, and J. Radford-Knoery (2004), Helium isotopes  
603 at the Rainbow hydrothermal site (Mid-Atlantic Ridge, 36°14'N), *Earth and Planetary Science Letters*,  
604 221(1-4), 325-335, doi: 10.1016/S0012-821X(04)00094-9.

605 Jean-Baptiste, P., E. Fourré, A. Dapoigny, J.-L. Charlou, and J. P. Donval (2008), Deepwater mantle 3 He  
606 plumes over the northern Mid-Atlantic Ridge (36°N-40°N) and the Azores Platform, *Geochemistry,*  
607 *Geophysics, Geosystems*, 9(3), 1-13, doi: 10.1029/2007GC001765.

608 Jean-baptiste, P., J. Charlou, M. Stievenard, J. P. Donval, H. Bougault, and C. Mevel (1991), Helium and  
609 methane measurements in hydrothermal fluids from the mid-Atlantic ridge : the Snake Pit site at 23° N,  
610 *Earth and Planetary Science Letters*, 106, 17-28, doi: 10.1016/0012-821X(91)90060-U.

611 Keir, R. S., J. Sültenfuß, M. Rhein, G. Petrick, and J. Greinert (2006), Separation of  $^3\text{He}$  and  $\text{CH}_4$  signals  
612 on the Mid-Atlantic Ridge at  $5^\circ\text{N}$  and  $51^\circ\text{N}$ , *Geochimica et Cosmochimica Acta*, 70, 5766-5778, doi:  
613 10.1016/j.gca.2006.06.005.

614 Kelley, D. S., and T. M. Shank (2010), Hydrothermal systems: A decade of discovery in slow spreading  
615 environments, in *Diversity of Hydrothermal Systems on Slow Spreading Ocean Ridges*, edited, pp. 369-  
616 407.

617 Kelley, D. S., et al. (2001), An off-axis hydrothermal vent field near the Mid-Atlantic Ridge at  $30^\circ\text{N}$ ,  
618 *Nature*, 412, 145-149., doi: Doi 10.1038/35084000.

619 Li, B., X. Shi, J. Wang, Q. Yan, and C. Liu (2018), Tectonic environments and local geologic controls of  
620 potential hydrothermal fields along the Southern Mid-Atlantic Ridge ( $12\text{--}14^\circ\text{S}$ ), *Journal of Marine*  
621 *Systems*, 181, 1-13, doi: 10.1016/j.jmarsys.2018.02.003.

622 Lupton, J. E. (1998), Hydrothermal helium plumes in the Pacific Ocean, *Journal of Geophysical Research:*  
623 *Oceans*, 103, 15853-15868, doi: 10.1029/98jc00146.

624 Lupton, J. E., and W. J. Jenkins (2017), Evolution of the south Pacific helium plume over the past three  
625 decades, *Geochemistry, Geophysics, Geosystems*, 18(5), 1810-1823, doi: 10.1002/2017GC006848.

626 Lupton, J. E., R. F. Weiss, and H. Craig (1977), Mantle helium in hydrothermal plumes in the Galapagos  
627 Rift, *Nature*, 267, 603, doi: 10.1038/267603a0.

628 McGillicuddy, D. J., J. W. Lavelle, A. M. Thurnherr, V. K. Kosnyrev, and L. S. Mullineaux (2010),  
629 Larval dispersion along an axially symmetric mid-ocean ridge, *Deep-Sea Research Part I: Oceanographic*  
630 *Research Papers*, 57(7), 880-892, doi: 10.1016/j.dsr.2010.04.003.

631 Melchert, B., et al. (2008), First evidence for high-temperature off-axis venting of deep crustal/mantle  
632 heat: The Nibelungen hydrothermal field, southern Mid-Atlantic Ridge, *Earth and Planetary Science*  
633 *Letters*, 275, 61-69, doi: 10.1016/j.epsl.2008.08.010.

634 Mercier, H., G. L. Weatherly, and M. Arhan (2000), Bottom water throughflows at the Rio de Janeiro and  
635 Rio Grande Fracture Zones, *Geophysical Research Letters*, 27(10), 1503-1506, doi:  
636 10.1029/2000GL011402.

637 Moalic, Y., D. Desbruyères, C. M. Duarte, A. F. Rozenfeld, C. Bachraty, and S. Arnaud-Haond (2012),  
638 Biogeography revisited with network theory: Retracing the history of hydrothermal vent communities,  
639 *Systematic Biology*, 61(1), 127-137, doi: 10.1093/sysbio/syr088.

640 Mullineaux, L. S., K. G. Speer, A. M. Thurnherr, M. E. Maltrud, and A. Vangriesheim (2002), Mullineaux  
641 et al., Implications of cross-axis flow for larval dispersal along mid ocean ridges, 2002.pdf, *Cahiers de*  
642 *Biologie Marine*, 43(3-4), 281-284, doi: <https://archimer.ifremer.fr/doc/00000/898/>.

643 Roether, W., R. Well, and A. Putzka (2001), Correction to "Component separation of oceanic helium",  
644 *Journal of Geophysical Research: Oceans*, 106(C3), 4679-4679, doi: 10.1029/1999JC000080.

645 Roether, W., R. Well, A. Putzka, and C. Rüth (1998), Component separation of oceanic helium, *Journal of*  
646 *Geophysical Research: Oceans*, 103, 27931-27946, doi: 10.1029/98jc02234.

647 Roether, W., M. Vogt, S. Vogel, and J. Sültenfuß (2013), Combined sample collection and gas extraction  
648 for the measurement of helium isotopes and neon in natural waters, *Deep Sea Research Part I:*  
649 *Oceanographic Research Papers*, 76, 27-34, doi: 10.1016/j.dsr.2013.02.006.

650 Rona, P. A., G. Klinkhammer, T. A. Nelsen, J. H. Trefry, and H. Elderfield (1986), Black smokers,  
651 massive sulphides and vent biota at the Mid-Atlantic ridge, *Nature*, 321, 33-37, doi: 10.1038/321033a0.

652 Rüth, C., R. Well, and W. Roether (2000), Primordial  $^3\text{He}$  in South Atlantic deep waters from sources on  
653 the Mid-Atlantic Ridge, *Deep Sea Research Part I: Oceanographic Research Papers*, 47, 1059-1075, doi:  
654 10.1016/S0967-0637(99)00077-1.

655 Ryan, W. B. F., et al. (2009), Global multi-resolution topography synthesis, *Geochemistry, Geophysics,*  
656 *Geosystems*, 10(3), doi: 10.1029/2008GC002332.

657 Saito, M. A., A. E. Noble, A. Tagliabue, T. J. Goepfert, C. H. Lamborg, and W. J. Jenkins (2013), Slow-  
658 spreading submarine ridges in the South Atlantic as a significant oceanic iron source, *Nature Geoscience*,  
659 6(9), 775-779, doi: 10.1038/ngeo1893.

660 Schmale, O., M. Walter, J. Schneider Von Deimling, J. Sültenfuß, S. L. Walker, G. Rehder, and R. Keir  
661 (2012), Fluid and gas fluxes from the Logatchev hydrothermal vent area, *Geochemistry, Geophysics,*  
662 *Geosystems*, 13(7), doi: 10.1029/2012GC004158.

663 Shank, T. M., D. J. Fornari, K. L. Von Damm, M. D. Lilley, R. M. Haymon, and R. A. Lutz (1998),  
664 Temporal and spatial patterns of biological community development at nascent deep-sea hydrothermal  
665 vents (9° 50'N, East Pacific Rise), *Deep-Sea Research II*, 45, 465-515, doi: 10.1016/S0967-  
666 0645(97)00089-1.

667 Sültenfuß, J., W. Roether, M. Rhein, J. Sültenfuss, W. Roether, and M. Rhein (2009), The Bremen mass  
668 spectrometric facility for the measurement of helium isotopes, neon, and tritium in water, *Isotopes  
669 Environ Health Stud*, 45, 83-95, doi: 10.1080/10256010902871929.

670 Tao, C., et al. (2011), Two hydrothermal fields found on the Southern Mid-Atlantic Ridge, *Science China  
671 Earth Sciences*, 54, 1302-1303, doi: 10.1007/s11430-011-4260-8.

672 Tao, C., et al. (2017), Hydrothermal plume mapping as a prospecting tool for seafloor sulfide deposits: a  
673 case study at the Zouyu-1 and Zouyu-2 hydrothermal fields in the southern Mid-Atlantic Ridge, *Marine  
674 Geophysical Research*, 38, 3-16, doi: 10.1007/s11001-016-9275-2.

675 Tivey, M. (2007), Generation of Seafloor Hydrothermal Vent Fluids and Associated Mineral Deposits,  
676 *Oceanography*, 20(1), 50-65, doi: 10.5670/oceanog.2007.80.

677 Van Dover, C. L., C. R. German, K. G. Speer, L. M. Parson, and R. C. Vrijenhoek (2002), Evolution and  
678 Biogeography of Deep-Sea Vent and Seep Invertebrates, *Science*, 295(2002), 1253-1257, doi:  
679 10.1126/science.1067361.

680 Visbeck, M. (2002), Deep Velocity Profiling Using Lowered Acoustic Doppler Current Profilers: Bottom  
681 Track and Inverse Solutions, *Journal of Atmosphere and Ocean Technology*, 19(section 2), 794-807, doi:  
682 10.1175/1520-0426(2002)019.

683 Walker, S. L., E. T. Baker, J. Resing, K. Nakamura, and P. McLain (2007), A new tool for detecting  
684 hydrothermal plumes: An ORP Sensor for the PMEL MAPR, paper presented at AGU Fall Meeting  
685 Abstracts.

686 Walter, M., C. Mertens, U. Stöber, C. R. German, D. R. Yoerger, J. Sültenfuß, M. Rhein, B. Melchert, and  
687 E. T. Baker (2010), Rapid dispersal of a hydrothermal plume by turbulent mixing, *Deep Sea Research Part  
688 I: Oceanographic Research Papers*, 57, 931-945, doi: 10.1016/j.dsr.2010.04.010.

689 Wang, H., X. Li, F. Chu, Z. Li, J. Wang, X. Yu, and D. Bi (2017), Mineralogy, geochemistry, and Sr-Pb  
690 isotopic geochemistry of hydrothermal massive sulfides from the 15.2° S hydrothermal field, *Journal of  
691 Marine Systems*, 180, 220-227, doi: 10.1016/j.jmarsys.2017.02.010.

692 Wang, S., H. Li, S. Zhai, Z. Yu, Z. Shao, and Z. Cai (2017), Mineralogical characteristics of polymetallic  
693 sulfides from the Deyin-1 hydrothermal field near 15°S, southern Mid-Atlantic Ridge, *Acta Oceanologica  
694 Sinica*, 36(2), 22-34, doi: 10.1007/s13131-016-0961-3.

695 Well, R., and W. Roether (2003), Neon distribution in South Atlantic and South Pacific waters, *Deep-Sea  
696 Research Part I: Oceanographic Research Papers*, 50, 721-735, doi: 10.1016/S0967-0637(03)00058-X.

697 Well, R., W. Roether, and D. P. Stevens (2003), An additional deep-water mass in Drake Passage as  
698 revealed by <sup>3</sup>He data, *Deep-Sea Research Part I: Oceanographic Research Papers*, 50(9), 1079-1098, doi:  
699 10.1016/S0967-0637(03)00050-5.

700 Wessel, P., W. H. F. Smith, R. Scharroo, J. Luis, and F. Wobbe (2013), Generic Mapping Tools:  
701 Improved Version Released, *Eos, Trans. Am. Geophys. Un.*, 94, 409-410, doi: 10.1002/2013EO450001.

702  
703

1

Supporting Information for

2

## **Locations and physico-chemical properties of several new discovered hydrothermal plumes above the Southern Mid-Atlantic Ridge (13°S-33°S)**

3

4

Florian Schmid<sup>1,2</sup>, Maike Peters<sup>3,4</sup>, Maren Walter<sup>1,3</sup>, Colin Devey<sup>2</sup>, Sven Petersen<sup>2</sup>, Isobel Yeo<sup>5</sup>, Janna Köhler<sup>3</sup>, John W. Jamieson<sup>6</sup>, Sharon Walker<sup>7</sup>, Jürgen Sültenfuß<sup>3</sup>

5

6

<sup>1</sup>MARUM, Center for Marine Environmental Sciences at the University of Bremen, Germany.

7

<sup>2</sup>GEOMAR, Helmholtz-Center for Ocean Research Kiel, Germany.

8

<sup>3</sup>IUP, Institute of Environmental Physics at the University of Bremen, Germany.

9

<sup>4</sup>ICBM, Institute for the Chemistry and Biology of the Marine Environment at the Carl von Ossietzky University of Oldenburg, Germany.

10

11

<sup>5</sup>National Oceanography Center Southampton, NOCS, UK.

12

<sup>6</sup>Memorial University of Newfoundland, St. John's, Canada

13

<sup>7</sup>NOAA/Pacific Marine Environmental Laboratory, Seattle, USA

14

Corresponding author: Florian Schmid ([fschmid@geomar.de](mailto:fschmid@geomar.de))

15

16

### **Contents of this file**

17

18

Texts S1 to S3

19

Figures S1 to S4

20

21 **Text S1. Calculation of Neon Anomalies**

22 Based on *Well & Roether (2003)* and *Kim et al. (2016)*, neon anomalies in the samples  
23 were calculated via

$$\Delta(\text{Ne}) = 100 \left[ \left( \frac{\text{Ne}_{\text{tot}}}{\text{Ne}_{\text{EQ}}(\text{T}, \text{S}, \text{P}_{\text{atm}})} \right) - 1 \right] [\%] \quad (1.1)$$

24 where  $\text{Ne}_{\text{tot}}$  is the measured neon concentration and  $\text{Ne}_{\text{EQ}}(\text{T}, \text{S}, \text{P}_{\text{atm}})$  is the adopted  
25 solubility equilibrium value at the observed potential temperature and salinity for standard  
26 atmospheric pressure (both in  $\frac{\text{cm}^3(\text{STP})}{\text{kg}}$ ). All  $\text{Ne}_{\text{EQ}}(\text{T}, \text{S}, \text{P}_{\text{atm}})$  values are based on the  $\text{Ne}_{\text{EQ}}(\text{T}, \text{S},$   
27  $\text{P}_{\text{atm}})$  values of *Weiss (1971)*.

28 **Text S2. Excess Air (EA) Correction of Helium Isotopic Data**

29 Step 1:

30 According to *Roether et al. (1998, 2001)*, oceanic helium can be separated into different  
31 components originating from different reservoirs. *Sültenfuß (1998)* found that there is no  
32 significant amount of tritiogenic helium in the South Atlantic and the crustal helium component  
33 is insignificant (*Stanley & Jenkins, 2013*) Hence, we will not consider these two sources of  
34 helium. Total measured amounts of  $^3\text{He}$  and  $^4\text{He}$  are given by the sum of components listed the  
35 following equations,

$$3\text{He}_{\text{tot}} = 3\text{He}_{\text{EQ}}(\text{T}, \text{S}, \text{P}_{\text{atm}}) + 3\text{He}_{\text{EA}} + 3\text{He}_{\text{Mantle}} \quad (1.2)$$

$$4\text{He}_{\text{tot}} = 4\text{He}_{\text{EQ}}(\text{T}, \text{S}, \text{P}_{\text{atm}}) + 4\text{He}_{\text{EA}} + 4\text{He}_{\text{Mantle}} \quad (1.3)$$

36 where  $3\text{He}_{\text{EQ}}(\text{T}, \text{S}, \text{P}_{\text{atm}}) + 3\text{He}_{\text{EA}}$  and  $4\text{He}_{\text{EQ}}(\text{T}, \text{S}, \text{P}_{\text{atm}}) + 4\text{He}_{\text{EA}}$  are the atmospheric  
37 components,  $3\text{He}_{\text{Mantle}}$  and  $4\text{He}_{\text{Mantle}}$  are primordial helium components originating from  
38 hydrothermal venting (all helium concentrations in  $\frac{\text{cm}^3(\text{STP})}{\text{kg}}$ ), and  $4\text{He}_{\text{EQ}}(\text{T}, \text{S}, \text{P}_{\text{atm}})$  is the  
39 solubility equilibrium value at the observed potential temperature and salinity for standard  
40 atmospheric pressure, which is calculated on the basis of  $4\text{He}_{\text{EQ}}(\text{T}, \text{S}, \text{P}_{\text{atm}})$  values from *Weiss*  
41 (*1971*).

42 Step 2:

43  $3\text{He}_{\text{EQ}}(\text{T}, \text{S}, \text{P}_{\text{atm}})$  is then derived as

$$3\text{He}_{\text{EQ}}(\text{T}, \text{S}, \text{P}_{\text{atm}}) = 4\text{He}_{\text{EQ}}(\text{T}, \text{S}, \text{P}_{\text{atm}}) R_A 0.984 \quad (1.4)$$

44 Where the last term gives the solubility equilibrium value of  $\delta^3\text{He}$ , exactly -1.6 %, in  
45 tropical waters due to air-sea gas exchange (*Benson & Krause, 1980*).

46 Step 3:

47 To separate the excess air (EA) components from the primordial components, the  
48 measurements of neon can be used. This procedure is valid since the only natural source of  
49 neon is the atmosphere, which contains on average 18.18 ppm<sub>v</sub> (parts per million based on the  
50 volume) of neon. The total amount of neon, Ne<sub>tot</sub>, is given via

$$\text{Ne}_{\text{tot}} = \text{Ne}_{\text{EQ}}(T, S, P_{\text{atm}}) + \text{Ne}_{\text{EA}} \equiv \text{Ne}_{\text{atm}} \quad (1.5)$$

51 (adapted from *Winckler, 1998*), where Ne<sub>EQ</sub>(T, S, P<sub>atm</sub>) is the adopted solubility  
52 equilibrium value at the observed potential temperature and salinity for standard atmospheric  
53 pressure and Ne<sub>EA</sub> is the EA component of neon (all concentrations in  $\frac{\text{cm}^3(\text{STP})}{\text{kg}}$ ). Since the ratio

$$\left(\frac{\text{Ne}}{4\text{He}}\right)_{\text{atmosphere}} = \frac{18.18}{5.24} = \left(\frac{\text{Ne}}{4\text{He}}\right)_{\text{EA}} \quad (1.6)$$

54 is constant in the atmosphere, it is possible to calculate the amount helium originating  
55 from EA using the following equations:

$$4\text{He}_{\text{EA}} = [\text{Ne}_{\text{tot}} - \text{Ne}_{\text{EQ}}(T, S, P_{\text{atm}})] \cdot \left(\frac{4\text{He}}{\text{Ne}}\right)_{\text{atmosphere}} \quad (1.7)$$

$$3\text{He}_{\text{EA}} = [\text{Ne}_{\text{tot}} - \text{Ne}_{\text{EQ}}(T, S, P_{\text{atm}})] \cdot \left(\frac{3\text{He}}{\text{Ne}}\right)_{\text{atmosphere}} \cdot R_A \quad (1.8)$$

56 The results of this correction are shown in Figure S1.

57

### 58 Quality assessment of the noble gas results

59 In total 810 samples (375 and 425 copper tubes) were analyzed and consecutively all  
60 samples were rejected if:

- 61 • The <sup>4</sup>He concentration of a sample was higher than  $6.5 \frac{\text{cm}^3(\text{STP})}{\text{kg}}$ , which is well  
62 above the solubility equilibrium of 4He in seawater (*Weiss, 1971*). <sup>4</sup>He  
63 concentrations above this value indicate excess air in the sample either  
64 introduced by air bubbles (near ocean surface) or during the gas extraction or  
65 mass spectrometry procedures.
- 66 • The Ne concentration of a sample is lower than  $15 \frac{\text{cm}^3(\text{STP})}{\text{kg}}$  in depths shallower  
67 than 900 dbar or lower than  $17 \frac{\text{cm}^3(\text{STP})}{\text{kg}}$  in depths deeper than 900 dbar. Such  
68 low Ne concentrations are implausible for South Atlantic waters according to  
69 *Well and Roether (2003)*, and would lead to spurious results of the excess air  
70 correction.
- 71 • The excess air correction resulted in a negative Ne<sub>EA</sub> value which is physically  
72 invalid.

73

74 **Text S3. References cited in Text S1 and S2**

75 Benson B.B. & D. Krause Jr. (1980): Isotopic Fractionation of Helium During Solution: A  
76 Probe for the Liquid State. *Journal of Solution Chemistry*, 9, 12, 895-909.

77 Kim I., D. Hahm, T.S. Rhee, T.W. Kim, C.-S. Kim & S.H. Lee (2016): The Distribution of  
78 Glacial Meltwater in the Amundsen Sea, Antarctica, Revealed by Dissolved Helium and Neon.  
79 *Journal of Geophysical Research Oceans*, 121, 3, 1,654–1,666, doi:10.1002/2015JC011211.

80 Lupton, J. E. (1983), Terrestrial inert gases: Isotope tracer studies and clues to primordial  
81 components in the mantle, *Annu. Rev. Earth Planet. Sci.*, 11(1), 371–414,  
82 doi:10.1146/annurev.ea.11.050183.002103.

83 Roether, W., R. Well, A. Putzka, and C. R uth (1998), Component separation of oceanic  
84 helium, *J. Geophys. Res.*, 103(C12), 27931–27946, doi:10.1029/98JC02234.

85 Roether, W., R. Well, A. Putzka, and C. R uth (2001), Correction to “Component  
86 separation of oceanic helium” by Wolfgang Roether, Roland Well, Alfred Putzka, and Christine  
87 R uth, *J. Geophys. Res.*, 106(C3), 4679, doi:10.1029/1999JC000080.

88 Stanley, R. H. R., and W. J. Jenkins (2013), Noble Gases in Seawater as Tracers for  
89 Physical and Biogeochemical Ocean Processes, in *The Noble Gases as Geochemical Tracers*,  
90 *Advances in Isotope Geochemistry*, edited by P. G. Burnard, pp. 55–79, Springer, Berlin,  
91 Heidelberg.

92 S ltenfu , J. (1998), Das Radionuklid Tritium im Ozean: Messverfahren und Verteilung  
93 von Tritium im Suedatlantik und im Weddellmeer, PhD Thesis, Institute of Environmental  
94 Physics, University of Bremen, Bremen.

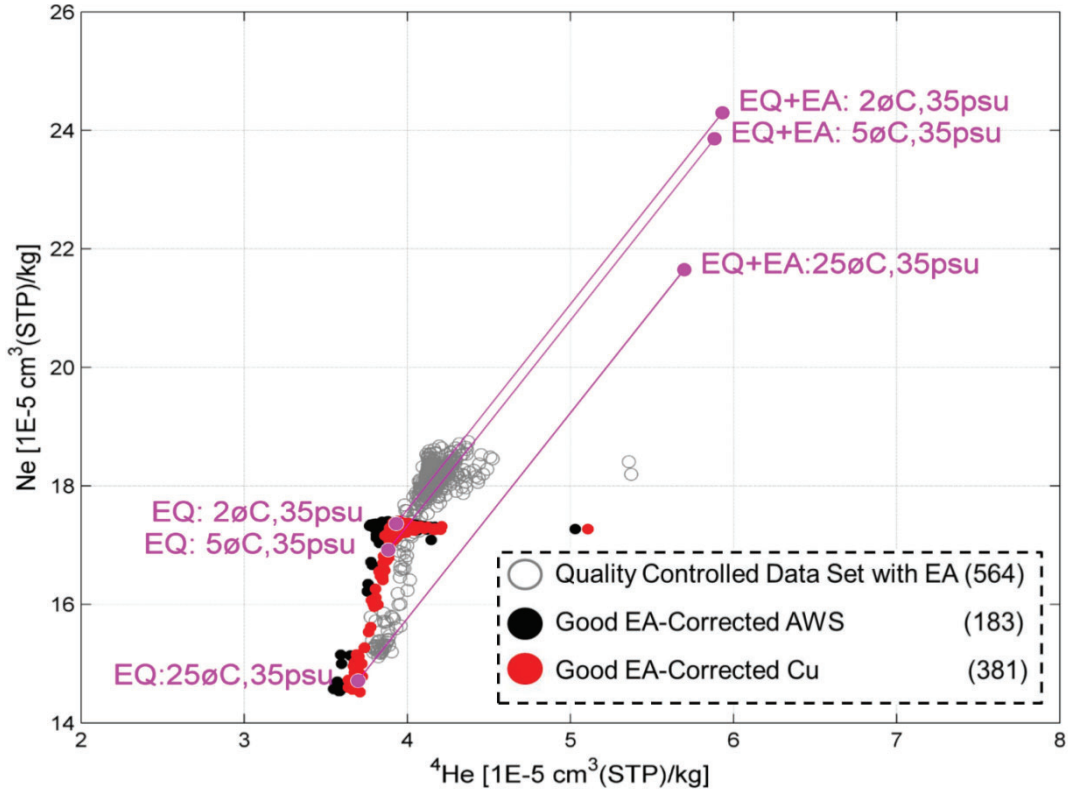
95 S ltenfu , J., W. Roether, and M. Rhein (2009), The Bremen mass spectrometric facility  
96 for the measurement of helium isotopes, neon, and tritium in water, *Isotopes in environmental  
97 and health studies*, 45(2), 83–95, doi:10.1080/10256010902871929.

98 Weiss R.F. (1971): Solubility of Helium and Neon in Water and Seawater. *Journal of  
99 Chemical and Engineering Data*, 16, 2, 235-241, doi: 10.1021/je60049a019.

100 Well, R., and W. Roether (2003), Neon distribution in South Atlantic and South Pacific  
101 waters, *Deep Sea Research Part I: Oceanographic Research Papers*, 50(6), 721–735,  
102 doi:10.1016/S0967-0637(03)00058-X.

103 Winckler G. (1998): Radiogenes Helium im Ozean - Drei Fallstudien. PhD Thesis,  
104 University of Heidelberg, Germany, ISBN:978-3-89722-082-9, 151pp.

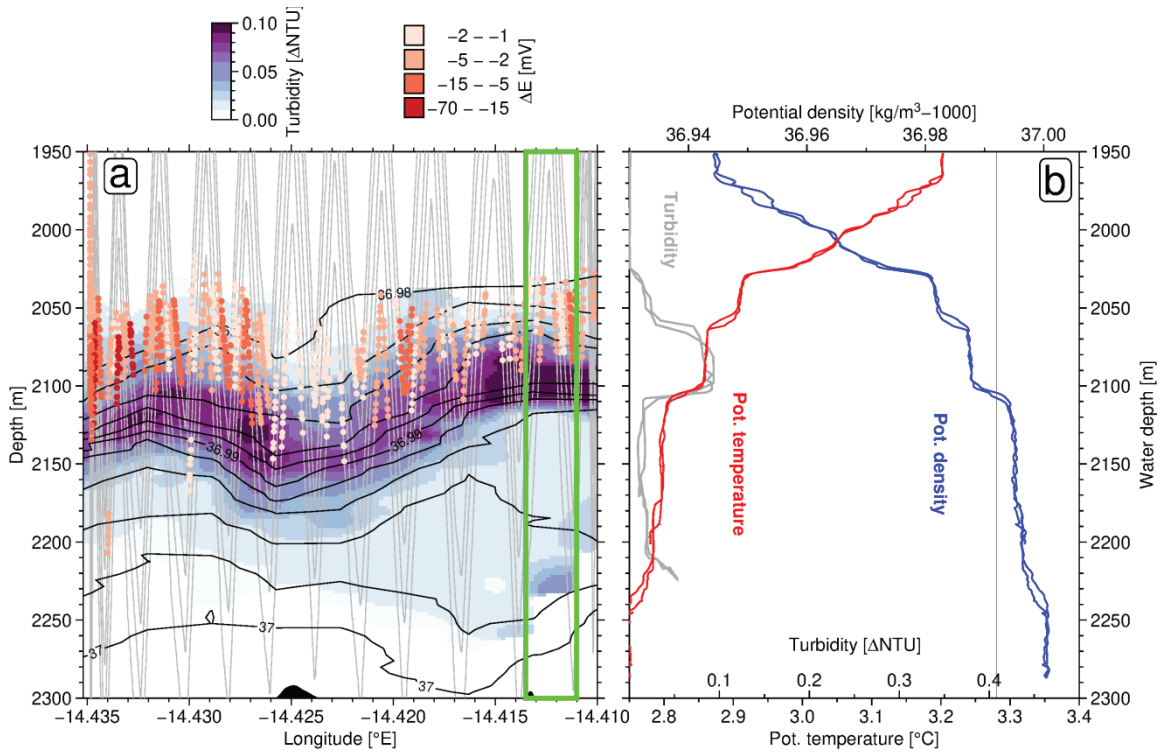
105



106

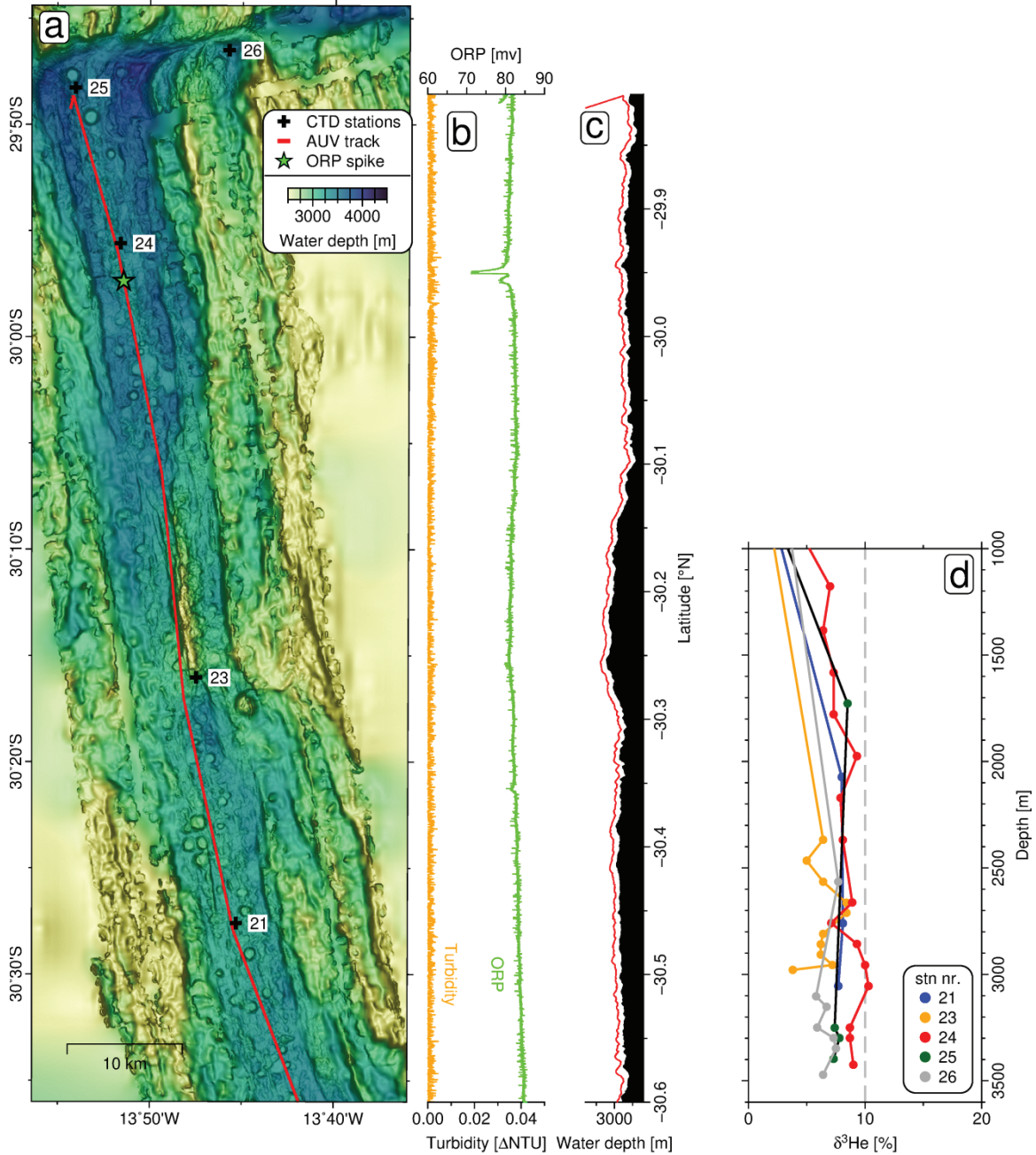
107 **Figure S1.** Measured  ${}^4\text{He}_{\text{tot}}$  versus  $\text{Ne}_{\text{tot}}$  with grey circles showing values uncorrected for excess  
 108 air (EA). Magenta points show examples for  ${}^4\text{He}_{\text{EQ}}$  vs.  $\text{Ne}_{\text{EQ}}$  values and  ${}^4\text{He}_{\text{EQ}}+{}^4\text{He}_{\text{EA}}$  vs.  $\text{Ne}_{\text{EQ}}+\text{Ne}_{\text{EA}}$   
 109 values at the coldest (2°C), the average (5°C) and the warmest (25°C) temperature of the study  
 110 area at a salinity of 35 psu. Three outliers of unusually high  ${}^4\text{He}$  and Ne values are affected by  
 111 large amounts of excess air. Red and black points show EA corrected AWS and Cu data points  
 112 with good data quality. In parentheses is the number of samples.

113



114  
 115  
 116  
 117  
 118  
 119  
 120  
 121  
 122  
 123  
 124

**Figure S2.** Relations of the neutrally buoyant plume above the Zouyu Ridge (13°S) and the local ocean stratification. Panel a, results from the NE-SW striking part of tow-yo 124 (tow track is plotted in Figure 3b of the main manuscript). Faint gray lines indicate MAPR tracks, the blue shading scales with turbidity, red dots show ORP anomalies, scaling with  $\Delta E$  and black contours are isopycnals. Panel b, profiles of potential density, potential temperature and turbidity for the region within the green rectangle in panel a. The vertical black line shows the  $36.992 \text{ kg m}^{-3}$  isopycnal, coinciding with the lower boundary of the particle plume. Note, the densest particle plume is confined between two stairs in the density, at 2060-2108 m depth. The ORP plume partly overlaps with the turbidity plume and reaches higher to the top of the overlying step in density.



126

127 **Figure S3.** Results from the 29°47'S – 30°40'S segment. Map a, bathymetry of the ridge segment  
 128 with AUV track and CTD stations. Panel b, turbidity and ORP versus latitude along the AUV track.  
 129 Panel c, vehicle- and seafloor depth versus latitude along the AUV track. Panel d, vertical profiles  
 130 of  $\delta^3\text{He}$  for stations 21 and 23-26. Note, that the ORP anomaly detected by the AUV near  
 131 29°57.4'S/13°51.4'W was not considered as unequivocal sign of hydrothermal activity in here  
 132 but may nonetheless hint diffuse venting.